

**SEARCH FOR JET QUENCHING IN Pb-Pb COLLISIONS AT  $\sqrt{s_{NN}} = 2.76$  TeV**

**Adrian Nassirpour**

Department of Physics, Division of Particle Physics, Lund University

Bachelor thesis supervised by Peter Christiansen



**LUND**  
UNIVERSITY

## ABSTRACT

The purpose of this thesis is to further investigate the state of matter known as Quark-Gluon Plasma (QGP) that is produced in heavy ion collisions. This is done by analyzing jets and jet quenching in Pb-Pb collisions at  $\sqrt{s_{NN}} = 2.76$  TeV from ALICE. The events are discriminated by setting a  $8 \text{ GeV}/c$   $p_T$  threshold on the trigger particle. This ensures that there is hard scattering inside

the collision. The jet quenching is hypothesized to occur in central collisions (0-5% centrality), whereas peripheral collisions (60-80% centrality) are used in order to form a good baseline. Projections are drawn from every track onto the trigger particle, in order to measure the relative  $p_T$  intensity for each collision. The results from the analysis conclude that there are significant anomalies of low- $p_T$  tracks in the 0-5% data compared to the baseline. This is likely correlated to soft gluon emission due to jet quenching.

# Populärvetenskaplig sammanfattning

## Adrian Nassirpour

Inom fysikens värld finns det väldigt många olika grenar som fördjupar sig inom väldigt specifika aspekter av fysiken. Tillsammans med alla dessa grenar så kan en helhetsförståelse av naturens lagar bildas; från den allra minsta molekylen, till stjärnor ljusår ifrån. Partikelfysik är den gren inom fysiken som undersöker vad som händer på den minsta skalan av materia. Ämnet beskriver hur fundamentalpartiklar (så som kvarkar) växelverkar och binder ihop till hadroner, grundstenarna av all materia.

Genom att accelerera hadroner upp till 99% av ljusets hastighet (snabbare än 1,000,000,000 km/h!) och kollidera dem med varandra så kan kvarkarna bryta sig ut från hadronerna. Man kan då studera hur kvarkarna påverkar varandra under kollisionen, samt undersöka vad det är som binder kvarkarna innan kollisionen. Det krävs enorma maskiner, kallade acceleratorer, för att hadronerna skall kunna uppnå dessa hastigheter. Kollisionerna som är analyserade i denna rapport sker mellan tunga bly partiklar, och kommer från CERN, mer specifikt deras accelerator "a Large Hadron Collider" (LHC).

Om kollisionen mellan hadronerna är kraftfulla nog, så kan kvarkarna bilda vad man kallar en Kvark-Gluon Plasma. Detta är ett tillstånd av materia som har väldigt hög temperatur (över 2 triljoner grader) och/eller densitet, där kvarkarna inte längre är bundna till individuella hadroner, utan istället flyter runt som en perfekt vätska. Det är detta tillstånd man tror befann universum befann sig i under en bråkdelens sekund, samt det man tror är kärnan av stora neutron stjärnor.

Problemet med att försöka observera kvark-gluon plasman är att den bara existerar under ett litet tidsintervall; bara bråkdelens sekunder efter kollisionen så kommer plasman kylas ner, och kvarkarna kommer förseglas innuti hadroner. För att kunna hitta tecken på kvark-gluon plasman så måste man då undersöka om, och hur, den påverkar de resterande partiklarna och hadronerna.

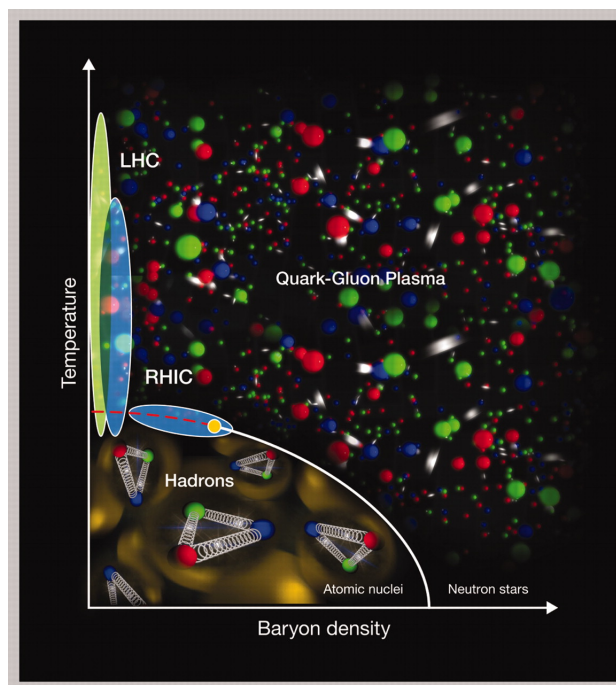


Figure 1: Illustration för hur kvark-gluon plasman förhåller sig till hadroner, samt visar vilka temperaturer som kan uppnås i acceleratorerna RHIC & LHC [1].

[1] Barbara V. Jacak, Berndt Müller, "The Exploration of Hot Nuclear Matter", published in Science, 2012. <http://www.sciencemag.org/content/337/6092/310.full>

## ACKNOWLEDGMENTS

Firstly, I would like to thank my supervisor, Peter Christiansen, for giving me the opportunity to do undertake this project, as well for his guidance and support throughout the project, from start to finish. Secondly, I would like to thank David Silvermyr, Anders Oskarsson and Evert Stenlund for elaborate explanations of the more convoluted aspects of particle physics. A big thanks to Vytautas Vislavičius, Martin Ljunggren and Tuva Richert for helping me throughout the project, with questions pertaining to both physics and programming. I would also like to thank Maria Mårtenson for both her help and feedback during the project.

Finally, an additional thanks to everyone that proof-

read the thesis paper and provided feedback:

- Peter Christiansen
- David Silvermyr
- Anders Oskarsson
- Adam Johansson
- Justin Eads
- Vytautas Vislavičius
- Martin Ljunggren

## CONTENTS

<b>I. Introduction</b>	2
<b>II. Theory</b>	3
A. The Standard Model	3
B. Quantum Chromodynamics	4
C. Hadrons, Baryons and Mesons	5
D. Proton-Proton Collisions	5
E. Jet events	5
F. Quark-Gluon Plasma	6
G. Jet Quenching/Jet Suppression	6
<b>III. Heavy Ion Collisions</b>	7
A. Phenomenology for Heavy-Ion Collisions	7
1. Multiplicity & Centrality	7
2. Azimuthal and Polar angles	8
3. Transverse Momentum	8
4. Rapidity and Pseudo-rapidity	9
B. LHC & ALICE	9
C. Time Projection Chamber	11
D. Inner Tracking System	11
<b>IV. Method</b>	12
A. Event-Plane for Trigger Particle	12
B. A Brief Explanation of the CMS study	14
<b>V. Results</b>	15
<b>VI. Discussion</b>	22
<b>VII. Conclusion</b>	22
<b>VIII. Bibliography</b>	23

## I. INTRODUCTION

The main purpose of this analysis is to further investigate the deconfinement of quarks. The notion of observing deconfined quarks has been a conundrum ever since the framework of the strong interaction, Quantum Chromo Dynamics (QCD), had been laid out. The deconfinement of quarks is studied through the formation of Quark-Gluon Plasma (QGP). The QGP can only form through large induced energy densities, such that the quarks deconfine due to thermal excitations, or are compressed such that no distinct bounds confine them. It is impossible to study the QGP on macroscopic levels; the energy density required is simply too large to artificially produce it. This is not the case on the microscopic scale. It is possible to attain the required energy density needed to form the QGP by accelerating and colliding heavy ions at the speed of light. The QGP will form, but is not stable, and will expand, cool down and produce ordinary hadrons throughout a small window of time. Therefore it is not possible to directly observe the formation of the QGP. Instead, signatures of the QGP are only found by observing auxiliary effects from the heavy ion collisions.

The heavy ion collisions will exhibit different characteristics depending on the momentum transfer during the collision. If the momentum transfer is high, the quarks within the ions will undergo hard scattering, to produce showers of particles. These showers are known as particle jets. If the collision creates a large enough energy density to form a QGP, the particle jets would have to travel through it. During its path through the QGP, the energy of the jet will reduce as it is constantly emitting radiation, due to the stopping force from the QGP. This process is known as jet quenching.

If two collisions are then compared, one with a large energy density, and one with a low energy density, a quenched jet would be associated to the formation of the QGP. This analysis will study jet quenching with data of Pb-Pb heavy ion collision, with an invariant center-of-mass energy of  $\sqrt{s_{NN}} = 2.76$  TeV from A Large Ion Collider Experiment (ALICE), at the European Organization for Nuclear Research (CERN). The framework of this particular analysis is inspired by a similar study performed by the Compact Muon Solenoid (CMS)<sup>1</sup> experiment at CERN. The results from the CMS study will be compared to the ones found in this thesis, in order to validate the method, and to gain further insight into where the jet quenching is located.

## II. THEORY

### A. The Standard Model

The Standard Model (SM) is a theoretical framework that unifies three out of the four fundamental forces at the subatomic level; the strong interaction (which is explained in more detail during the following section), the weak interaction and the electromagnetic interaction (through Quantum Electro Dynamics, QED). The fourth fundamental force, gravity, is expected to be negligible in the sub-atomic scale. Hence it will not be discussed further.

The SM is built around 29 elementary particles. The interactions between them can be explained through a combination of the three fundamental forces. Within the 29 particles, 24 are fermions (12 particles + 12 anti-particles), whereas 5 are bosons. The fermions are further divided into two smaller sub-groups; quarks and leptons. As seen in Fig. 1, each of the 12 fermions have their unique mass and, except for the neutrino particles, electric charge. The fermions and leptons are further narrowed down to three separate generations. One can note that the scale of mass increases for each concurrent generation.

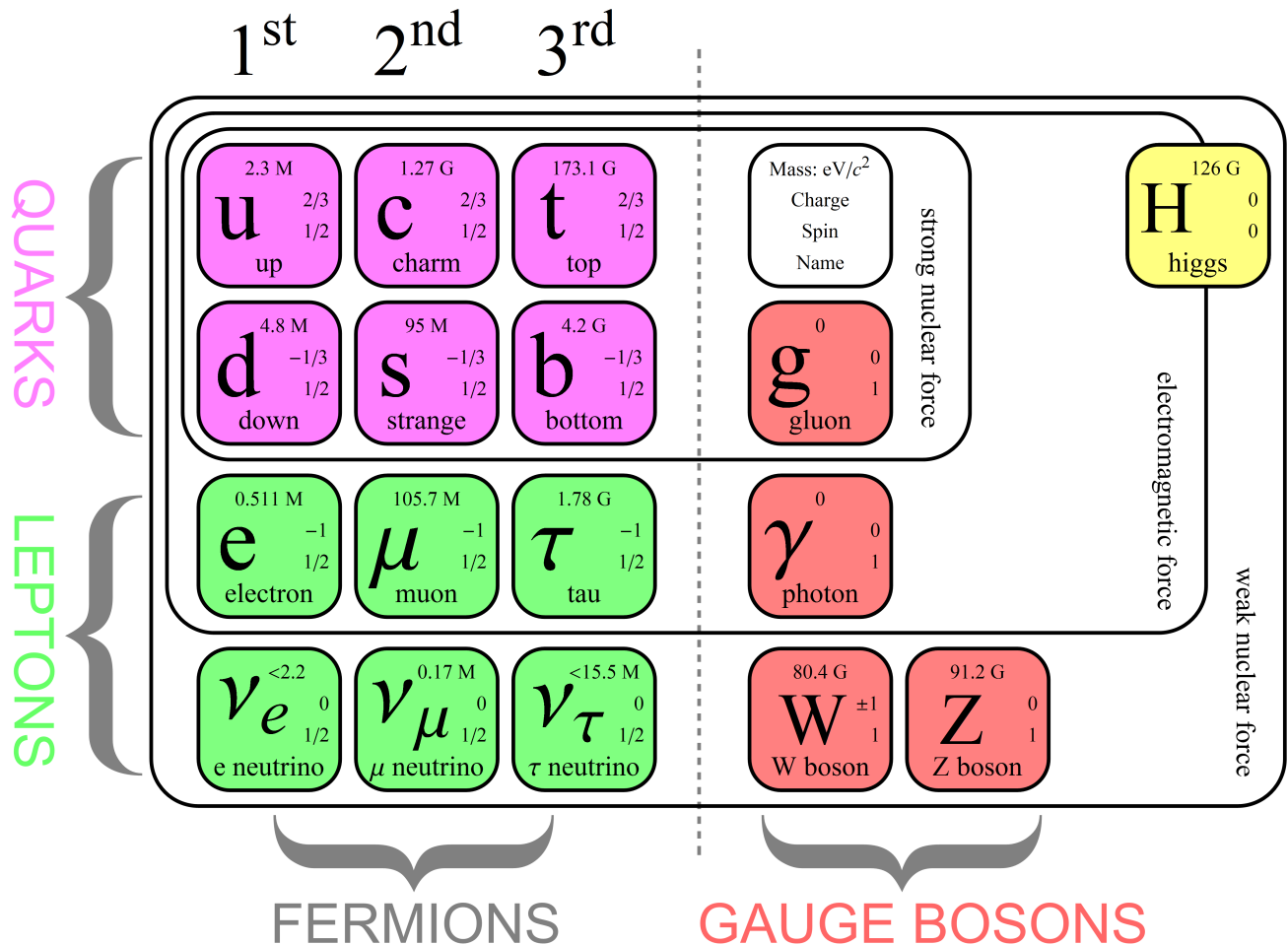


FIG. 1. Elementary particles, quarks, leptons and bosons that make up the Standard Model. The figure also illustrates which particles are affected by the three different fundamental particle interactions.<sup>2</sup>

While Fig. 1 only portrays 12 fermion particles, there is also a corresponding anti-particle to each fermion. The differences between the particles and the corresponding anti-particles are that the quantum numbers are opposite (electric polarity, lepton numbers etc); the mass still remains the same.

In contrast to the fermions, the bosons are spin-0 and spin-1 particles. In turn, they are not bound by the Pauli-exclusion principle. There are currently four known

spin-1 gauge bosons, and one spin-0 scalar boson<sup>3</sup>. The gauge bosons are considered the mediator particles of the three fundamental interactions. The photon is the electric charge mediator, the gluon the mediator of the strong force and the  $W^{\pm}/Z^0$  bosons mediate the weak interaction. The scalar boson is known as Higgs boson. Being the latest addition to the SM, the discovery of the Higgs boson laid to rest one of the more glaring problems within the SM. In order to treat weak and electromagnetic inter-

actions similarly, it was theorized that the  $W^\pm/Z^0$  had to be massless, just as the photon. However, experimental data suggested otherwise, so something had to assign mass to the  $W^\pm/Z^0$  bosons in order for the model to hold. The Higgs mechanism was theorized as the responsible mechanism for creating the additional mass.<sup>4</sup>

## B. Quantum Chromodynamics

Quantum Chromodynamics (QCD) describes the strong interaction, one of the four fundamental forces. It contains the fundamental theory of quarks and gluons (together known as partons).

There are currently 6 known quarks, divided into 3 different generations, each quark with its unique mass. The quarks make up 50% of the fermions in the SM. The quarks are further evenly divided into two groups; either having  $\frac{1}{3}$  or  $-\frac{2}{3}$  units of the elementary charge ( $1.602 \cdot 10^{-19}C$ )<sup>5</sup>.

Gluons, on the other hand, are the particle mediators for the strong interaction. The gluons and quarks are each assigned a color charge. The partons carry this color charge, and the gluons mediate the strong force analogously to how the photon mediates the electromagnetic force from QED. A large difference comparing the photon to the gluon is that the gluon itself can carry a charge of what it mediates, a color charge. This gives rise to a term known as color confinement.

The color charge is needed in order to ensure the Pauli-exclusion principle for the quarks. However, in contrast to QED (which only accounts for positive and negative charges), the color charges range from Red, Green or Blue, and their respective anti-states; anti-Red, anti-Green or anti-Blue. The quarks are charged with one of the colors, the anti-quarks are charged with one of the anti-colors, and the gluon is charged with both a color and an anti-color. Furthermore, colored particles by themselves are not observable (and can not be isolated)<sup>6</sup>, they are only observable when the color charge is neutral<sup>7</sup>. While the gluons interact and mediate colors to surrounding quarks and gluons, the total color charge is always conserved (illustrated in Fig. 3).

As gluons are also color charged they may interact with other gluons. The effect of gluons self-interacting leads to another peculiar phenomena; asymptotic freedom<sup>8</sup>. Asymptotic freedom is based on the effect that the strength of the strong interaction gets weaker the closer the quarks are, and stronger the further the quarks are pulled apart. The reason for why the strong interaction diminishes the closer the two quarks are, is due to an effect known as anti-screening.

Analogous to how electrons screen of each other due to quantum fluctuations (pair productions and annihilation) in QED, gluons can also screen each other during similar quantum fluctuations. However, since the gluons also interact with each other, a gluon self-interaction can occur during their pair production. The gluons will then anti-screen the quarks, and probability of emitting radiation increases as the distance between the quarks decreases (at larger momentum transfers). An increased

probability of radiation means that less color is concentrated at the quarks. As the color concentration decreases, the quarks will act more like free particles<sup>9</sup>. So the strength of the strong interaction diminishes over short distances<sup>10</sup>.

The strength of the interaction, as well as the asymptotic freedom, is also described through the coupling constant for the strong force. The coupling constant  $\alpha_s$  for the strong interaction is:

$$\alpha_s(Q) = \frac{16\pi^2}{11 - \frac{2}{3}N_f \ln[\frac{Q^2}{\Lambda^2}]} \quad (1)$$

Where  $Q$  is the squared energy-momentum transferred during the interaction (which is used as a Lorentz-invariant generalization of the momentum transfer<sup>11</sup>),  $N_f$  the amount of quarks active in the resulting pair production, and  $\Lambda$  a scale parameter set to around 0.2 GeV. The scale parameter is chosen such that it is calibrated by the coupling constant at the mass of the  $Z^0$  boson.<sup>12</sup>

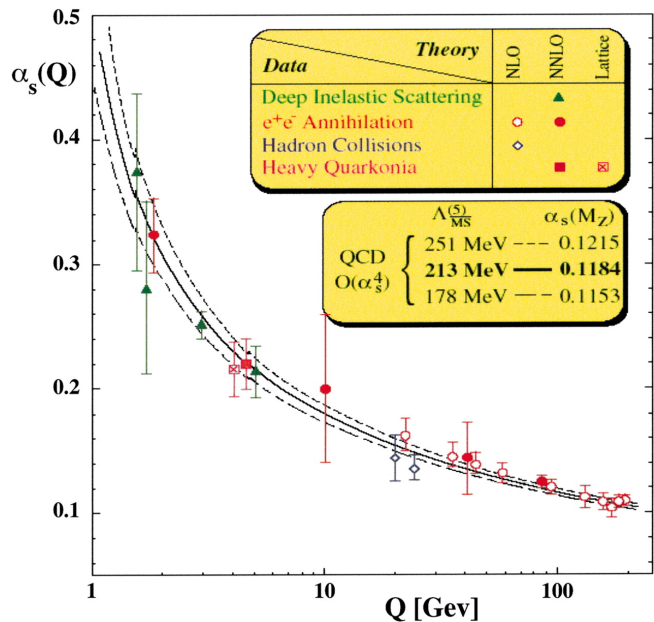


FIG. 2. Display of how the coupling constant for the strong interaction changes depending on  $Q$ . As seen in the graph, the phenomena is consistent with QCD throughout all the different interactions presented in the graph.<sup>13</sup>

Studying Fig. 2 and the coupling constant for the strong interaction, one can note that the coupling constant rises as  $Q$  becomes smaller, but diminishes as  $Q$  increases. This is interpreted to being due to color confinement when the momentum transfer is small, such that the quarks are tightly bound. When the momentum transfer is large, the quarks almost act like free particles. So the asymptotic freedom depends on a relation of both distance, and the value of  $Q$ .

The strong coupling constant is measured experimentally rather than analytically. Analytically, less is known about the color confinement compared to the asymptotic

freedom. QCD calculations can be done in the region of asymptotic freedom, using perturbation theory with good accuracy, whereas the color confinement is limited<sup>6</sup>.

### C. Hadrons, Baryons and Mesons

Historically, hadrons, such as protons and neutrons, were considered fundamental particles. This understanding changed, as both experimental, as well as theoretical, discrepancies were found that contradicted the possibility of protons and neutrons being fundamental particles. It became evident, when experiments on deep inelastic scattering of electrons on hadrons were performed at the SLAC<sup>14</sup>, suggesting that the hadrons had to have an internal structure.

Hadrons, are built out of different configurations of quarks. The hadrons have to consist of a quark configuration such as the total color charge becomes neutral. This allows the quarks composition, for example a proton, to have two up-quarks and still abide the Pauli exclusion principle.

The hadrons are defined by the configuration of the quarks inside it. One can split the hadron "family" into two more narrowly, well defined groups; mesons (consisting of a quark-anti quark pair) and baryons (consisting of either three quarks or three anti-quarks). Depending on the configuration of the quarks, both baryons and mesons can either be positive, negative or neutrally charged. However, both baryons and mesons must have a quark configuration such that the total charge is either in discrete units of  $\pm 1$  or 0 of elementary charge, as well as having a neutral color charge.

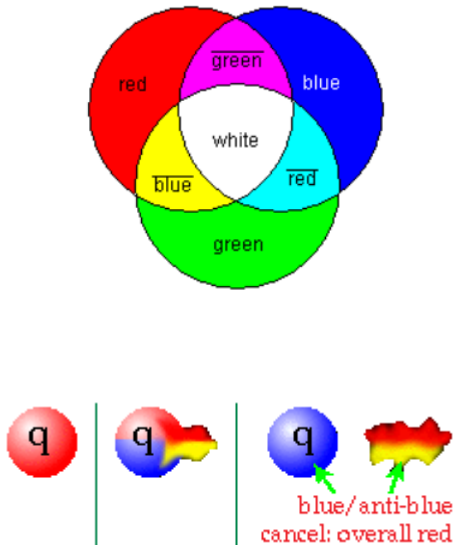


FIG. 3. A figure illustrating the different colors for the strong interaction (top), as well as showing how the color flavor for a contained system, whilst emitting a gluon, is conserved (bottom).<sup>15</sup>

### D. Proton-Proton Collisions

Understanding the mechanics of proton-proton (p-p) collisions is important, as it is one of the most fundamental hadron collisions. The collision between protons can rather be seen as direct collisions between the bound quarks and gluons. There are, in general, two different processes that occur in p-p collisions; hard scattering & soft scattering.

The hard scattering is associated with large Q-transfers, and is coupled to the rightmost component of Fig. 2. During large momentum transfers, the coupling constant is small, and the quarks act as virtually free particles. The quarks will then violently scatter on impact. These collisions are non-elastic, and will scatter at large angles, perpendicular to the direction of incident. Hard scattering is responsible for phenomena such as jets (further explained in section II-E).

Soft scattering is associated with small Q-transfers, and can be coupled to the leftmost part of Fig. 2. During small momentum transfers, the quarks will stay bound inside the hadrons. The quarks are then essentially blind to each other, and will have a low probability of scattering. In contrast to the hard scattering, these collisions are mostly elastic.<sup>16</sup> Soft scattering is responsible for color exchange between protons, where gluon string fields (further discussed in II-E) are created between the two protons. Soft scattering is also accountable for phenomena such as bulk particle production & hydrodynamic flow. This concept is not entirely relevant to this thesis, but further reading can be found<sup>17</sup>.

If there were no additional QCD mediums or mechanics present for heavy ion collisions, a heavy ion collision between two nuclei should behave like a scaled-up pp collision. The scaling would depend on the amount of protons from the two nuclei that actually interact with each other. This number is known as the amount of binary collisions  $N_{\text{Coll}}$  that occur throughout the nuclei collision, and is calculated using Glauber modeling<sup>18</sup>.

For example, if an interaction between two gold nuclei (Au-Au) is observed, the 79 protons from one gold nucleus will not interact with every proton in the other gold nucleus. Otherwise  $N_{\text{Coll}}$  would equal 6241 collisions. This is not reflected in the experimental data, where simulations show that  $N_{\text{Coll}}$  for (Au-Au) is  $\sim 1000$  for a large overlap between the nuclei, and down to  $\sim 10$  for glancing collisions<sup>19</sup>. This is useful, as one can study QCD phenomena by comparing if there are any significant characteristics that are present in the nuclei-nuclei collision, but missing in the p-p collision.

### E. Jet events

As described in the previous section (II-B), quarks are strongly bound together by gluons due to color confinement. It is, however, possible to sever the bond by exerting large quantities of energy upon a particle (i.e colliding them in an accelerator). If the momentum transfer is large, quarks considered as free for a small window of time, and will then either recombine with the quarks

from its original hadron, or instead undergo hadronization. During hadronization, the quark spontaneously creates a rapid shower of new hadrons in a tight cone. The shower of hadrons is associated with a hard scattered parton referred to as a particle jet.

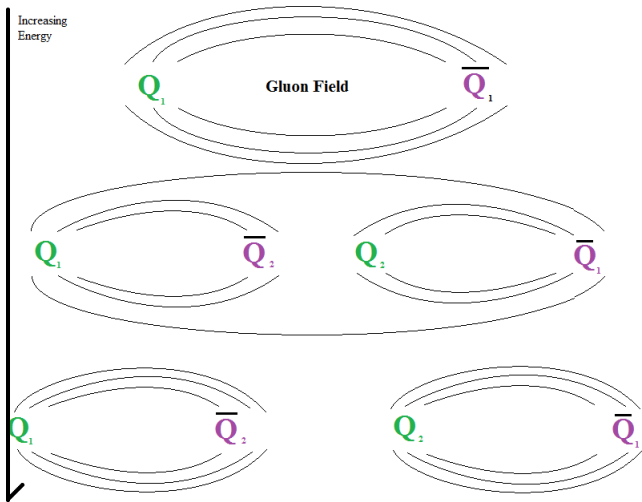


FIG. 4. The string-quark model, displaying how new particles are created as the gluon fields are pulled apart. For jet events, this process is repeated until the original energy is dissipated.

This process is best explained in more detail by the quark string model; The energy stored in the gluon field in between two bound quarks,  $Q_1$  and  $\bar{Q}_1$ , will increase as the two quarks are being separated. When the two quarks are sufficiently separated, the gluon field will contain enough energy to spontaneously create two additional quarks (akin to QED pair-creation),  $Q_2$  and  $\bar{Q}_2$ . However, as the two new quarks are created, the binding gluons and corresponding gluon fields will alter.  $Q_1$  will now be bound to  $\bar{Q}_2$ , and  $\bar{Q}_1$  will be bound to  $Q_2$ , creating two new mesons from the original meson<sup>6</sup>.

Hadronization is inherently a soft process; while the quarks drift apart from each other, a gluon field is spanned between them. Hadrons are then spontaneously created as the field expands, distributed isometrically around the collision. However, if a hard scattering occurs in the collision, large quantities of energy, from the non-elastic collision, will deposit into the gluon field. The energy is large enough to create "chain reactions" of this process; the two newly defined gluon fields will split and create four additional quarks, with a total of 4, well-defined gluon fields. The process is illustrated in Fig. 4 above, and will keep repeating until the initial energy is dissipated, creating a shower of hadrons in the process<sup>20</sup>.

The outcome of a hard collision will create jets, which focus large cones of the hadronization into directions perpendicular to the beam axis. As the quarks arrive with a well-defined momentum along the beam-axis before the collision, two opposite jets are created in order to conserve momentum. Such an event is defined as a di-jet event, where the larger jet is defined as the main-leading jet, whereas the other is defined as the sub-leading jet. As the presence of jets is easily identifiable, and only occur

for hard scatterings, they can be used in order to discriminate if the observed collision contains a hard scattering. If clear, high-energetic jets are present, the collisions had to contain at least one hard scattering.

## F. Quark-Gluon Plasma

Based on the QCD principle of color charge, colored particles, such as the gluons and quarks, have to be confined and cannot be directly nor independently observed. However, a state of matter was hypothesized where the quarks and gluons could be deconfined from their hadron shells. This new state of matter, which is referred to as the QGP, would be incredibly dense and is theorized to be present in the core of heavy neutron-stars. Furthermore, it is proposed that the Universe existed as a Quark-Gluon Plasma for a couple of microseconds just after the Big Bang<sup>21</sup>.

However, to test and verify the practical existence of this proposed new state of matter would prove to be difficult. In order to create the QGP, either tremendous amounts of energy (in form of temperature/heat) needs to be induced to excite the quarks out from the hadron shells, or large amounts of pressure needs to be applied in order to "merge" together the hadrons (seen in Fig. 5).

It is not possible to create QGP on a macroscopic scale; the required temperatures or pressures are simply too large to artificially produce it. The only way of currently observing the formation of QGP is to measure auxiliary effects from particle collisions.

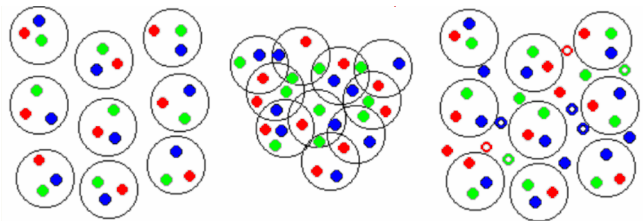


FIG. 5. A figure illustrating the confinement and the deconfinement of quarks and gluons. In the left most image, the quarks and gluons are confined within hadron shells. The quarks are then deconfined when the pressure is increased and the hadronic shells merge together (middle), or when temperature is increased allowing the quarks to move freely (right).<sup>22</sup>

## G. Jet Quenching/ Jet Suppression

Jet quenching, or jet suppression, is an exhibited phenomena that heavily suggests the formation of a QGP in heavy-ion collisions. Results from RHIC<sup>23</sup> show that the sub-leading jets created by heavy ion collisions behaved differently depending if the collision was central or peripheral. As seen in Fig. 7, the main jet at  $\Delta\phi = 0$  radians (the azimuthal angle  $\phi$  is further explained in section

III-A-2), produced from Au-Au collisions, behaves similarly to p-p collisions at both 0-5% centrality and 60-80% centrality. However, the sub-leading jets, placed approximately  $\pi$  radians away from the main jet, only exhibit p-p like characteristics for collisions at 60-80% centrality. For the 0-5% centrality case, the tracks at  $\Delta\phi \approx \pi$  have a severely reduced energy compared to the 60-80% centrality case<sup>21</sup>.

This is called jet quenching, and can be interpreted together with the formation of the QGP. When the colliding nuclei completely overlap, enough heat and pressure is supplied in order to create the QGP. As illustrated in Fig. 6, the sub-leading jet will have to travel through the QGP. While doing so, the jet will emit radiation, analogous to electron Bremsstrahlung. The gluon bremsstrahlung is hypothesized to be dominated by soft gluon emission and radiated in small, but frequent, doses in order to halt the partons moving through the plasma. Thus, through energy loss during the gluon bremsstrahlung, the sub-leading jet will not be as energetic compared to a collision where the QGP is not formed.

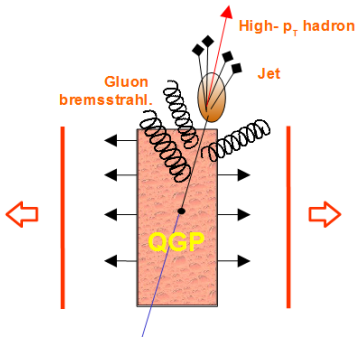


FIG. 6. Illustration of a jet travelling through a quark-gluon plasma. As the figure illustrates, gluon bremsstrahlung is radiated from the jet as it traverses the plasma. The amount of gluon radiation emitted depends on the density of the plasma.<sup>22</sup>

To identify jet quenching, the Nuclear Modification Factor,  $R_{AA}$ , of the particle yield is defined<sup>25</sup>.

$$R_{AA} = \frac{\text{Yield in A-A}}{N_{Coll} \cdot \text{Yield in p-p}} \quad (2)$$

$R_{AA}$  exhibits if the production mechanism in A-A collisions is the same as in a p-p collision. If there is no QCD medium (for example, the QGP) within the A-A collision, the production should be as a p-p collision multiplied by the amount of nucleon collisions equivalent,  $N_{Coll}$ , to the A-A collision. Thus the value of  $R_{AA}$  for any given experiment will tell if the jets are quenched, enhanced or unmodified compared to a p-p collision, which is illustrated in Fig. 8.

$$\begin{aligned} R_{AA} < 1 &\rightarrow \text{Jet Quenching} \\ R_{AA} = 1 &\rightarrow \text{Unmodified} \\ R_{AA} > 1 &\rightarrow \text{Jet Enhancement} \end{aligned}$$

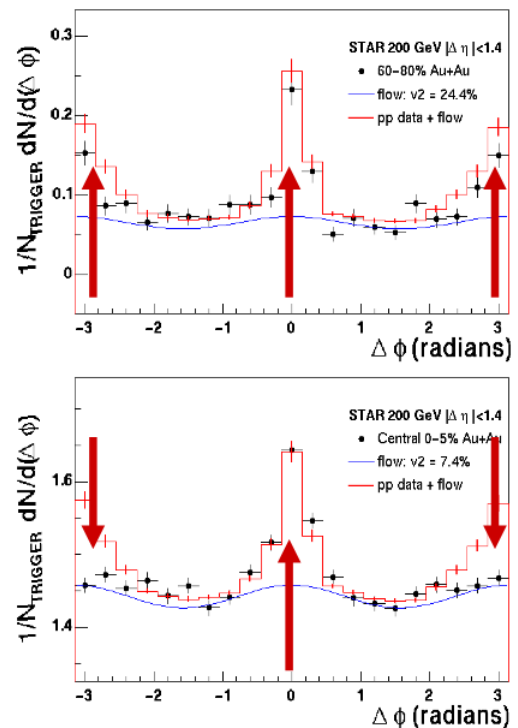


FIG. 7. Data from RHIC, illustrating how the sub-leading jet from Au-Au collision of low centrality behave differently compared to p-p collisions and high-centrality Pb-Pb collisions.<sup>23</sup>

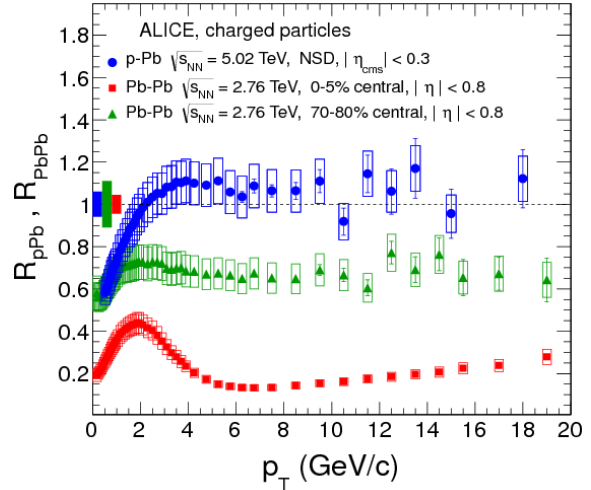


FIG. 8.  $R_{AA}$  data for different collisions measured by ALICE. According to the  $R_{AA}$ , the data indicates that there is jet quenching for Pb-Pb collisions, especially central ones.<sup>24</sup>

### III. HEAVY ION COLLISIONS

#### A. Phenomenology for Heavy-Ion Collisions

##### 1. Multiplicity & Centrality

Colliding nuclei will have different scales of the momentum transfer depending on how much the two nuclei overlap. A large overlap (known as a central collision)

will lead to a larger  $N_{\text{Coll}}$  and a larger momentum transfer, whilst the result of a small overlap (known as a peripheral collision) would do the opposite. The portion of particles that take part in the collision are known as participants, whereas the particles that do not collide are known as spectators. This behavior can be seen in Fig. 9.

However, the particle detectors can not microscopically observe the overlap between the two nuclei. Instead, the number of particles that scatter throughout the detector is counted. This is known as the multiplicity of the collision.

The multiplicity is then divided into different intervals. These intervals are defined by how the total distribution of events is compared to the multiplicity. For example, between some arbitrary number A corresponding to a percentile of the multiplicity distribution, versus the amount of recordings of the largest multiplicity, would be:

$$C = \frac{\int_A^{N_{Tmax}} \frac{dN_E}{dN_T} \times dN_T}{\int_0^{N_{Tmax}} \frac{dN_E}{dN_T} \times dN_T} \quad (3)$$

Where C is defined as the centrality of the collision,  $N_T$  is the number of tracks and  $N_E$  is the number of events.

The multiplicity and centrality are what represents the overlap between the two colliding nuclei. An event with high multiplicity contains a high amount of participants, so there would have to be a large amount of overlap. The centrality represents the amount of participants for each collision, and through Glauber modeling, the length of the impact parameter  $b$  (the distance between the two center of masses) between the two colliding ions<sup>26</sup>.

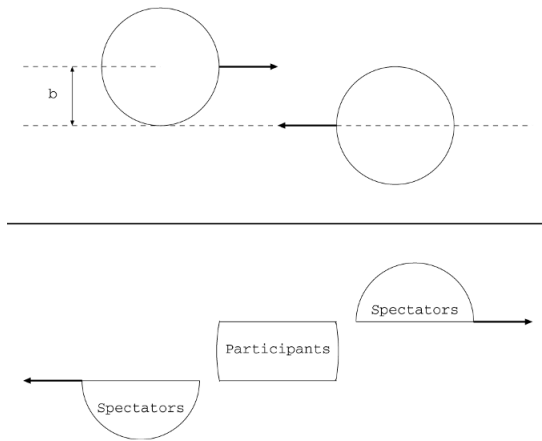


FIG. 9. The concept of participant particles and spectating particles. Each section acts like a "sack" of particles.<sup>22</sup>

## 2. Azimuthal and Polar angles

For cylindrical coordinates, two angles are measured for each particle track. The polar angle  $\theta$ , is the longitudinal angle between the beam-line and the particle track. In Cartesian coordinates, assuming the z-direction is along the beam-line, it represents the angle from the

z-axis to the particle track. Thus the scattering angle is used in order to represent phenomena occurring parallel to the beam-line.

In contrast, the azimuthal angle  $\phi$  is defined as the horizontal angle between a track and an arbitrary axis, around the beam-line. As Fig. 10 illustrates, one could imagine the azimuthal angle behaving the same as the angle around the unit circle. In Cartesian coordinates, assuming that the z-direction is along the beam-line, it represents the angle from the x-axis or the y-axis to the particle track.

## 3. Transverse Momentum

One of the key variables to observe during a high-energy physics experiment is the momentum, and how it is conserved, throughout the system. Particle detectors are often concentrically built around the particle beam-axis. Thus, the momentum of the particles that scatter perpendicular to the beam-axis are easier to measure, and defined as the transverse momentum,  $p_T$ , of the corresponding particle. Mathematically, the transverse momentum is referred to as:

$$p_T = \sqrt{p_x^2 + p_y^2} \quad (4)$$

Where  $p_x$  and  $p_y$  are the Cartesian values of the momentum perpendicular to the beam-axis. Furthermore, the  $p_T$  for each particle is zero before the collision (the total momentum is focused along the beam axis), and non-zero throughout/after the collision. Observing the  $p_T$  for each particle is therefore giving a picture of what occurs during the collision.

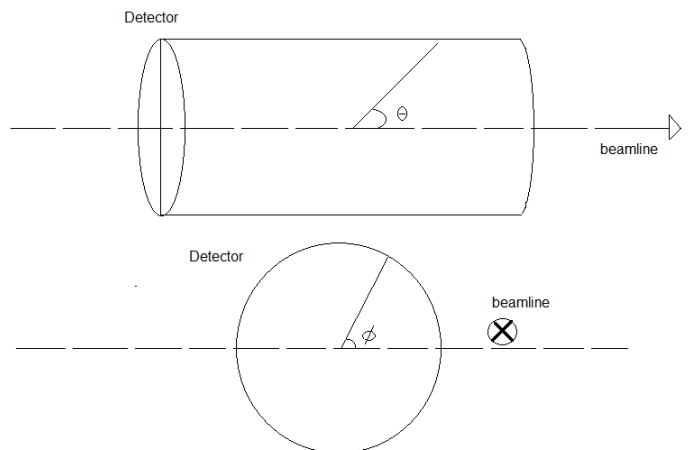


FIG. 10. Explanation of the azimuthal and polar angles in relation to the detector and the beamline.

#### 4. Rapidity and Pseudo-rapidity

In order to measure the linear components of the momentum, two new factors are introduced. Namely the rapidity and the pseudo-rapidity. The rapidity of the detector system is defined as<sup>27</sup>:

$$y = \ln \frac{E + p_z}{E - p_z} = \operatorname{arctanh} v_z \quad (5)$$

Where  $E$  is the energy of the particle ( $E = \sqrt{m^2 + \mathbf{p}^2}$ , where  $\mathbf{p}$  is the total momentum),  $p$  the different momentum components and  $v_z$  is the parallel velocity. As the particles in the accelerator move at relativistic speeds, it is thus more useful to measure the rapidity instead of the standard velocity. Furthermore, rapidity is Lorentz additive for boosts along the beam-axis. However, identifying (determining the mass) for each track is difficult. Hence approximation of the rapidity, namely pseudo-rapidity, is used instead. The pseudo-rapidity is defined as:

$$\eta = \frac{1}{2} \ln \frac{|\mathbf{p}| + p_z}{|\mathbf{p}| - p_z} = -\ln \tan\left(\frac{\theta}{2}\right) \quad (6)$$

Where  $\mathbf{p}$  and  $p_z$  are defined like the rapidity variables, and  $\theta$  is the scattering angle. Since the rapidity is Lorentz additive for boosts along the beam axis, assuming that pseudo-rapidity is a sufficient approximation of rapidity, then pseudo-rapidity will also be Lorentz additive. Thus, as the scattering angle is the easiest component to measure in the detector, pseudo-rapidity is the measurement of the linear, non-transverse components of the momentum. Furthermore, the pseudo-rapidity, together with the azimuthal angle, can now be used in order to define the momentum in Cartesian coordinates (assuming the z-direction along the beam-line):

$$\begin{aligned} p_x &= p_T \cos(\phi) \\ p_y &= p_T \sin(\phi) \\ p_z &= p_T \sinh(\eta) \end{aligned} \quad (7)$$

#### B. LHC & ALICE

The data presented in this report is gathered from the Large Hadron Collider (LHC), at the European Organization for Nuclear Research (CERN)<sup>28</sup> based in Geneva, Switzerland. The LHC is a particle synchrotron designed to accelerate protons & ions, collide them, and study what occurs during the collision. The LHC is currently the most powerful particle collider as of yet, accelerating protons up 6.5 TeV per beam. The accelerator

has a circumference of 27km, and uses over 1000 superconducting magnets in order to bend and focus along the beam line.<sup>29</sup> There are several experimental stations, built up with different particle detectors, that study collisions of the LHC. The particle beams collide against each other, in the middle of each experiment, such that the outcome of the collision can be observed. A schematic of LHC, and the rest of CERN, can be found in Fig. 11

Each experimental station is different from the other; each with its unique detector configuration, as well as what particle interactions are observed. The data that is presented in this report is from Pb-Pb collisions, at  $\sqrt{s_{NN}} = 2.76$  TeV, from A Large Ion Collider Experiment (ALICE). Like most high-energy experiments, ALICE is concentrically built around the beam-line, and is fitted with different detectors and components in a layered manner. In total, ALICE has an azimuthal coverage of  $2\pi$ , and a partial pseudo-rapidity coverage from approximately -4 to 5. However, the components that are built for momentum reconstruction only have a pseudo-rapidity coverage of -1.4 to 1.4<sup>30</sup>. A full schematic of ALICE is found in Fig. 12, but for the analysis performed in this report, there are two components from ALICE that are vital in order to track the particle jets; the Time Projection Chamber (TPC) and the Inner Tracking System (ITS).

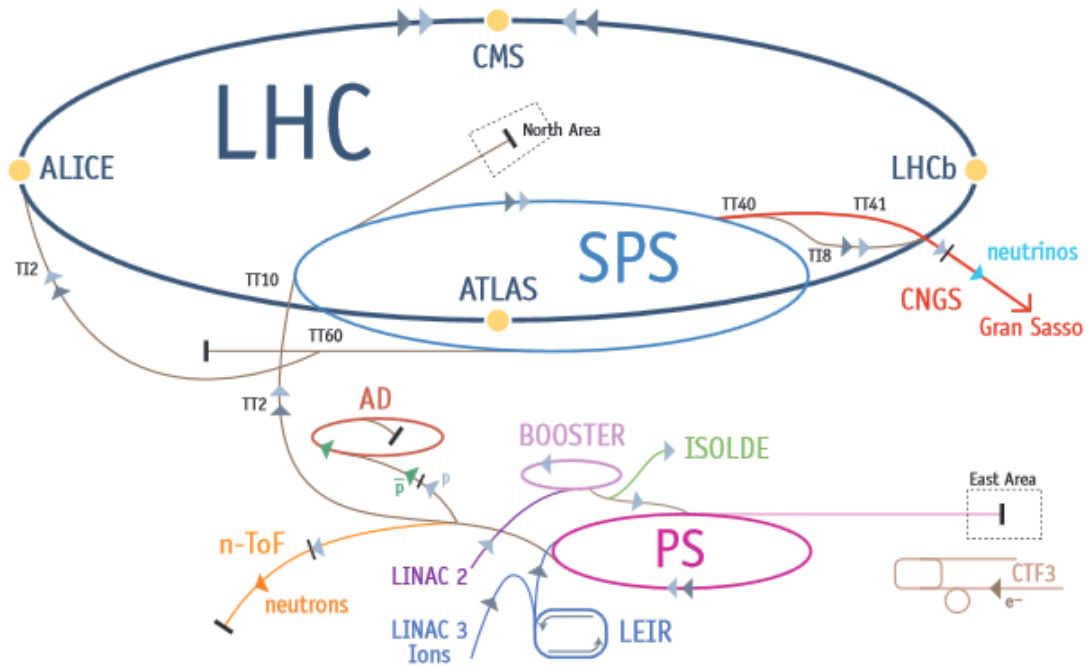


FIG. 11. An overview of the LHC and the different accelerators at CERN, detailing the various detectors and experiments.<sup>29</sup>

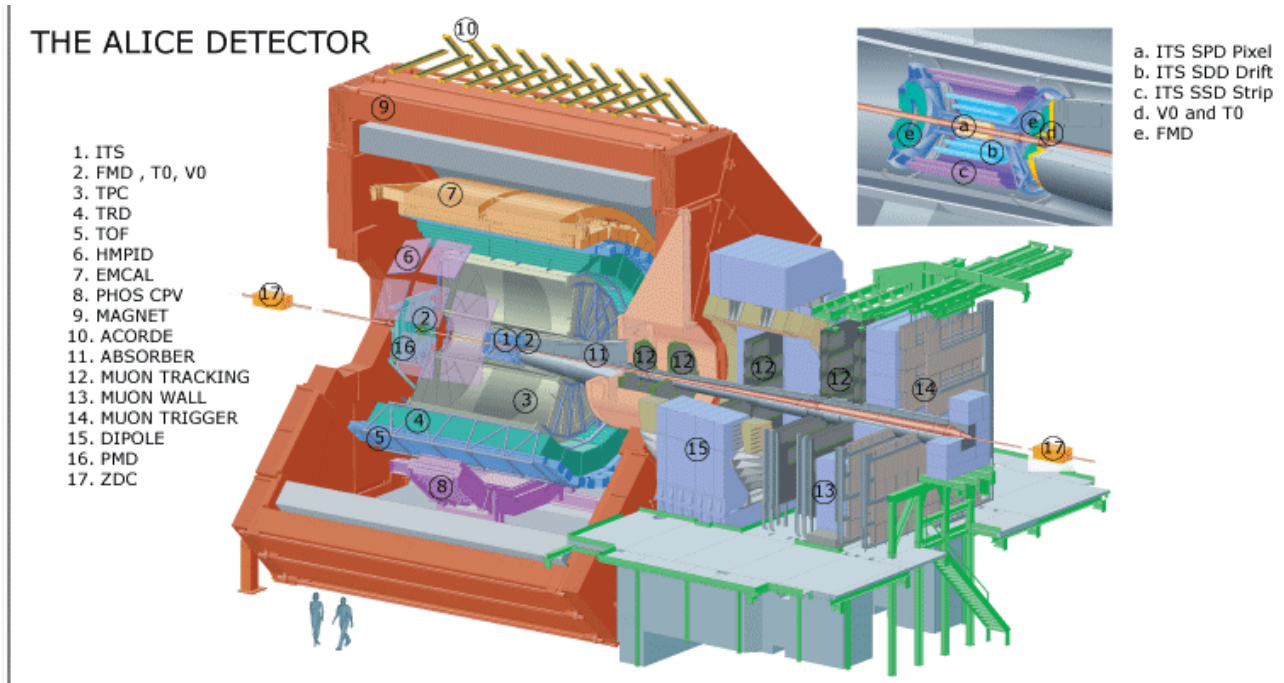


FIG. 12. An overview of ALICE and all its different components. The ones that are prevalent in this analysis are the ITS (see insert) and TPC detectors<sup>31</sup>.

### C. Time Projection Chamber

The TPC is one of the main components in ALICE, and is responsible for tracking both spatial location, as well as the  $p_T$  of each particle track. The TPC at first glance operates similarly to a classic, Multi-Wire Proportional Chamber (MWPC), gas detector. A MWPC detector is filled with a gas, and as the particles resulting from the collision enter the chamber, the gas will ionize. Wires running throughout the gas-volume will further amplify the signal from the ionization.

However, if one would want to determine the three spatial coordinates of any given particle with a classic MWPC, one would need to configure the wires into two crossing layers. However, this would not be feasible if there are several, simultaneous, tracks for each event, which is indeed the case for ALICE. This is due to the fact that if two or more particles were to enter detector simultaneously, the detector would not be able to compute which wires correlate to which particle. Therefore the TPC does not have wires going through the gas-volume, but have MWPC's at the end chambers instead<sup>32</sup>, seen in Fig. 13. An electric field is applied through the gas (parallel to the beam-axis), as well as a magnetic field, where the electric and magnetic fields are parallel to each other.

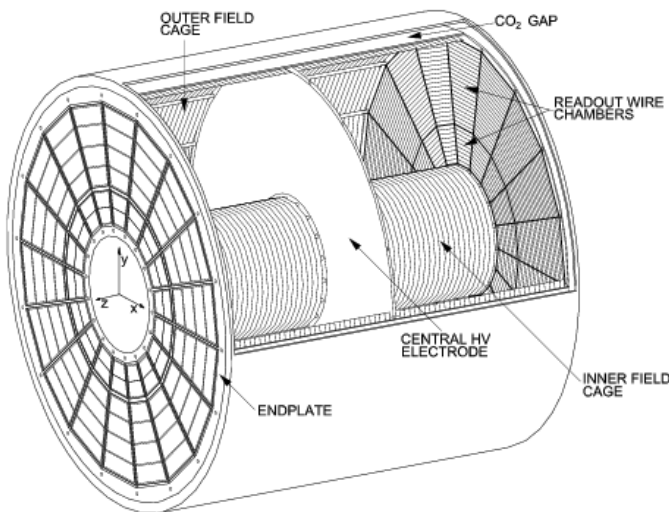


FIG. 13. Illustration of the TPC. The volume is filled with a gas mixture of  $\text{CO}_2$  and  $\text{Ne}$ .<sup>33</sup>

As the particles enter the gas in the TPC, the gas will ionize, and the resulting electrons will drift opposite of the electric field, towards the end chambers. It takes  $88\mu\text{s}$  for the electrons to drift from the central HV electrode to the MWPC chambers. The distance between the MWPC chambers and the HV electrode is 250cm, giving a approximate drift velocity of  $\frac{2.8\text{cm}}{\mu\text{s}}$ ,

While the electron drifts through the gas, there is probability that it will interact with the gas molecules and atoms due to diffusion. Hence the signal can be considered point-like at the initial ionization but will have a statistical uncertainty at the end-chambers, as the signal will spread out perpendicular to the beam axis. The

parallel magnetic field partially helps stabilize the diffusion process, as the electrons will start to spiral if they are scattered towards a different direction. The internal magnetic and electric field created by the drifting current are negligible compared to the external fields.

At the MWPC chambers, the signal will amplify through a series of electron avalanches. This determines the two spatial coordinates that are perpendicular to the beam-axis. The third spatial component is determined by measuring the drift time; by measuring the time it takes for the electrons to drift from the location of ionization to the end chambers.

By measuring the spatial coordinates, the TPC also measures the  $p_T$  for each particle track. It does so by measuring the gyroradius  $\rho$  for the electromagnetic rigidity  $R$ :

$$R = B \cdot \rho = p_T/q \quad (8)$$

Where  $B$  is the strength of the magnetic field and  $q$  the electric charge. Since the gyroradius can be measured in the TPC, the  $p_T$  can be defined for each track. However, this also restricts the accuracy of the TPC when measuring high momentum particles, as the particles will bend less due to the magnetic field the more momentum they have. In turn, the estimation of the gyroradius will become less accurate (as the particle track will resemble a straight line, more so than a curve), leading to a worse momentum estimation for the track.

While the TPC is generally more advanced than the standard MWPC, there are some drawbacks. For instance, the TPC requires a certain amount of time in between each pulse to reset. For purposes such as finding the Higgs boson, one would require 100k collisions per second in order to statistically produce 1 Higgs boson /day. Thus the TPC is more suited to collisions that may contain more tracks, but under a lower collision rate.

### D. Inner Tracking System

In addition to the TPC, the ITS is essential when tracking the  $p_T$  for any given particle track. The ITS is concentrically placed before the TPC, and its main purpose is to track the particle interaction vertexes that occur during collision. The ITS can track particles on the low-end of the momentum scale, around 0.1 GeV/c and under. Additionally, the ITS gives space points for each particle track, which helps in the global tracking of the collisions.

The ITS complements the TPC to give ALICE a good estimation of the momentum for each particle, from the low-end to the reasonably high-end (60-100 GeV/c) of the momentum spectra.

## IV. METHOD

The method performed for this thesis will be discussed in a step-by-step manner. The analysis is done with different programming algorithms using C++, with the ROOT data analysis framework. The geometry of the system can be hard to grasp, thus referring to Fig. 14 will help to visualize the method.

### A. Event-Plane for Trigger Particle

In order to probe the QGP through jet quenching, we observe the characteristics of a central collision and compare that to what occurs during a peripheral collision. Thus the following analysis is done for both 0-5% centrality, and 60-80% centrality. The expected jet quenching should occur in the 0-5% centrality collisions, with the

60-80% being a good baseline. Any exhibited signatures that are prevalent for the 0-5% centrality case, but does not appear in the 60-80% gives good ground for being the jet quenching mechanism.

The ALICE electromagnetic calorimeter has previously been used in order to track jets and their energies. However the method performed by this study is solely based of the results of the TPC and ITS. As with the aforementioned CMS<sup>1</sup> study, (which is briefly discussed in chapter IV-B) the relative  $p_T$  "strength" of the tracks alongside the main-leading jet are compared to the tracks opposite to the jet. If gluon brehmsstrahlung is dominated by soft gluon emission, the emitted gluon brehmsstrahlung should have a small  $p_T$  relative to the rest of the particle tracks. This analysis only accounts for the  $p_T$  of each particle, so the pseudo-rapidity of each particle is disregarded, as the transverse momentum is independent of the pseudo-rapidity. This is illustrated in Fig. 15.

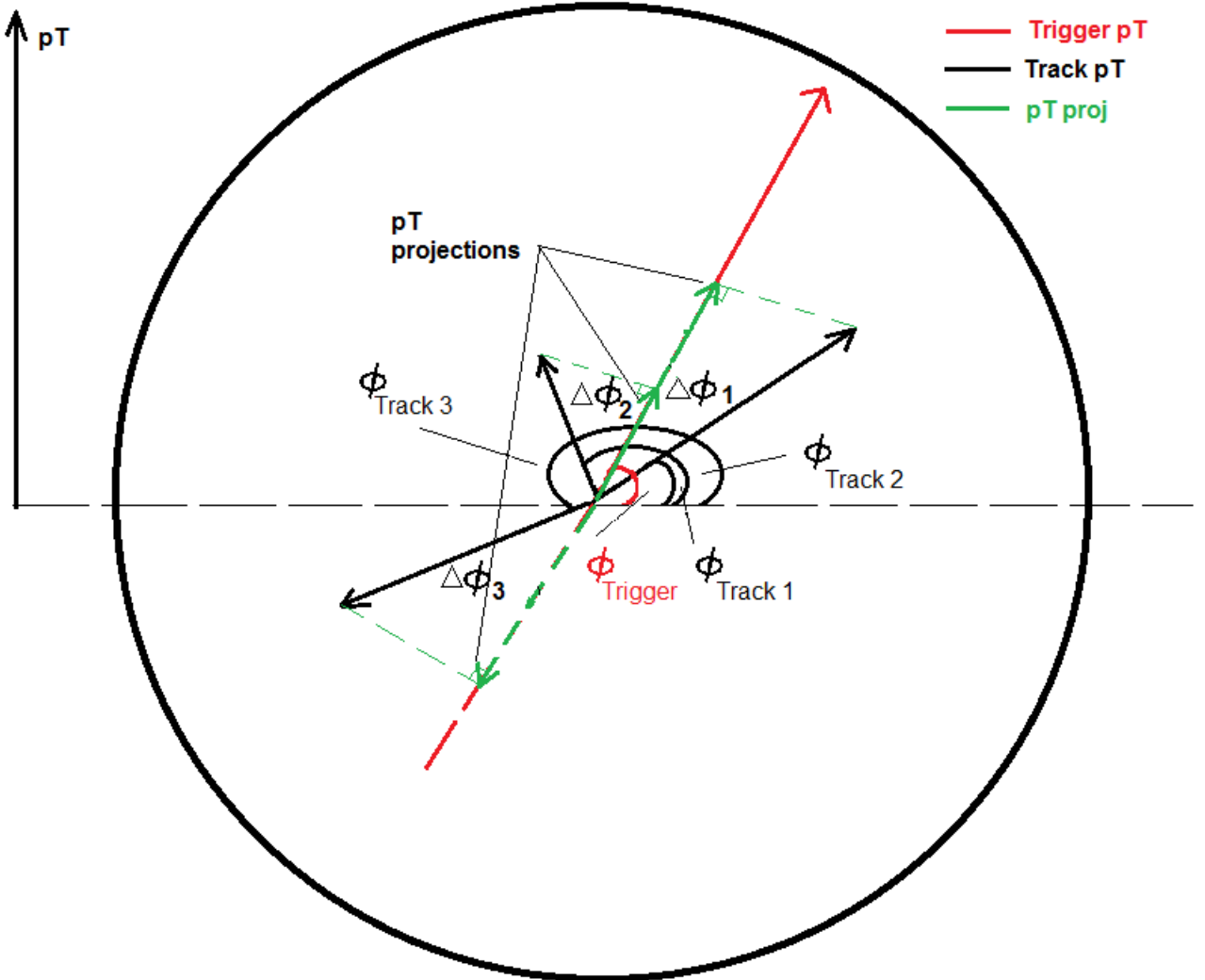


FIG. 14. An illustration of how the positioning of the different angles and  $p_T$  projections for a 4-track example. This process is repeated for every track that is generated throughout the collision, until every particle track has a  $\Delta\phi$  in relation to the trigger jet. Either positive or negative projections are then drawn, depending on what direction the particle track is pointing at relative to the trigger track.

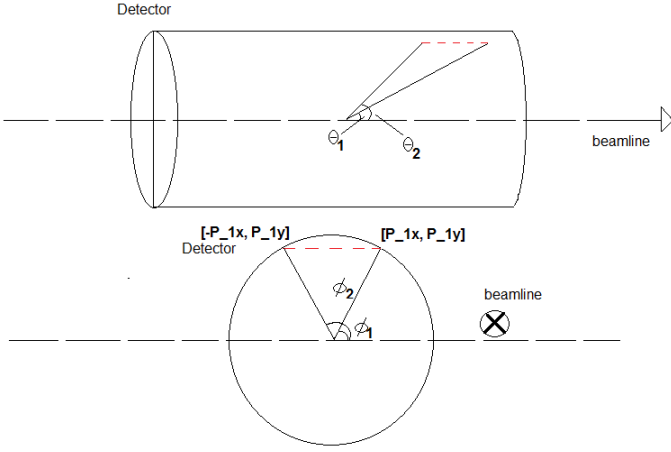


FIG. 15. The transverse momentum of two different tracks are independent of the scattering angle, and thus independent of the pseudo-rapidity.

In order to measure the relative  $p_T$  of all the tracks, the main-leading jet has to be selected for every event. Identifying the leading jet is no difficult task; one only needs to search for the highest  $p_T$  value for each given event. A threshold for each event is set such that the highest  $p_T$  value needs to exceed 8 GeV/c. If it does not, it is assumed that no jet was created during the collision, and the event is discarded. The main-leading jets that surpasses the threshold are referred to as the trigger particles. Once all the tracks are counted and the main (leading) jet is found, a plane is constructed around the main jet. This is done by taking the difference between the  $\phi$  for the jet track, and every other track in the event. In the new plane,  $\phi$  between all the tracks compared to the jet track are calculated as:

$$\Delta\phi = \phi_{\text{Jet}} - \phi_{\text{Track}} \quad (9)$$

Where the range for  $\Delta\phi$  is  $-\pi < \Delta\phi < \pi$ . Furthermore, once the plane is established, projections are drawn from each track to the main-leading jet. The main-leading jet is extrapolated into the opposite direction from the projections of the tracks opposite to the jet. The projections are defined as:

$$p_{T\text{-proj}} = p_T \cos \Delta\phi \quad (10)$$

Where  $p_T$  refers to the transverse momentum for each particle track.

Eq. 13 will thus provide with both positive (alongside the jet) and negative (away from the jet) projections. The projections are then tallied up into two different groups; the positive projections  $\frac{dN}{dp_{T\text{-proj}}^+}$  and the negative projections  $\frac{dN}{dp_{T\text{-proj}}^-}$ . If each collision event is isotropic, the average between the all the two different projections should be zero. The difference is taken between all the two different projections (i.e the difference in positive and negative bins for any given value larger than 8 GeV/c). The difference between all the projections is further normalized by the amount of trigger particles, and will display if there is an overshoot or undershoot, for any given value of  $p_{T\text{-proj}}$ .

Additionally, a more thorough analysis is done in order to establish the geometrical location, in relation to the main jet, of the the potential overshoot or undershoot of  $p_{T\text{-proj}}$ . This is done by segmenting the area around the jet into four different segments, as is seen in Fig. 16. An arc is created around the jet, such that it contains angles where  $|\Delta\phi| < 0.8$  radians. An identical arc is created opposite of the jet. The assumption is that the arc is wide enough to capture the sub-leading jet; in order to conserve momentum the two jets do not always have to be back-to-back. Ideally one would want to be able to construct cones such that  $\sqrt{|\Delta\phi|^2 + |\Delta\eta|^2} < 0.8$  instead of arcs. This can not be done, as the sub-leading jet is not localized, hence there is no guarantee that the sub-leading jet has to lie in the cone.

The two areas containing the jets are referred to two cones, whereas the rest is referred to as the bulk. In turn, a variable for the projections in each zone is created, two containing positive projections and two containing negative projections.

$$\begin{aligned} \text{Zone 1: } & \frac{dN}{dp_{T\text{-proj-cone}}^+} \\ \text{Zone 2: } & \frac{dN}{dp_{T\text{-proj-cone}}^-} \\ \text{Zone 3: } & \frac{dN}{dp_{T\text{-proj-bulk}}^+} \\ \text{Zone 4: } & \frac{dN}{dp_{T\text{-proj-bulk}}^-} \end{aligned} \quad (11)$$

The differences between the positive and negative projections for the bulk (Zones 3 & 4) areas, respectively for the cone areas (Zones 1 & 2), are taken. The idea is that discrepancies should be averaged out when taking the difference between the regions. If the collision would be entirely isometric, the differences between the positive and negative projections within each region should be zero.

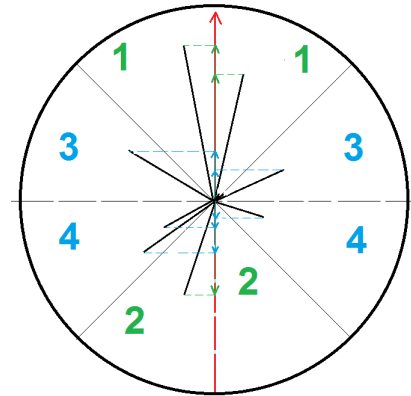


FIG. 16. Figure explaining how the different track projections are divided into two groups. Zones 1 and 2 are referred to as cones and only contains the "green" projections, whereas zones 3 and 4 are referred to as the bulk and only contain "blue" projections. The positive and negative green and blue projections are then compared independently of each other, so the difference in bulk would only contain blue projections, and the difference in cones would only contain green projections.

Finally, the different segments of the cones are examined, in order to identify the lack of/abundance of certain  $p_T$  projections lie. This is done by partitioning the cones into more finer areas, with a separation of 0.2 radians. An illustration of this is done in Fig. 17

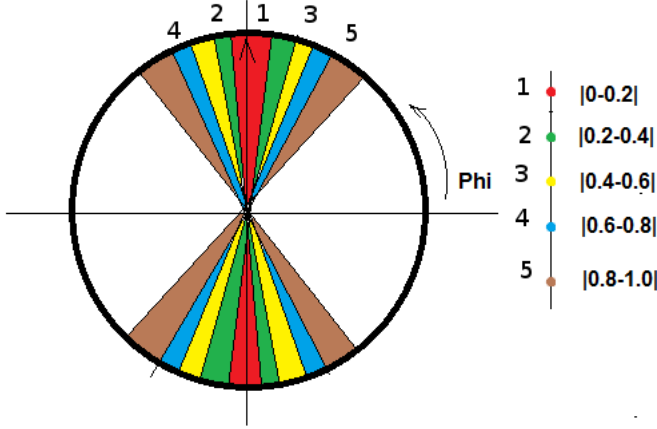


FIG. 17. The cones around the main jet are further divided down into more narrow areas. The numbers represents the segmented intervals of  $\Delta\phi$  in units of radians.

## B. A Brief Explanation of the CMS study

The method used in the CMS study<sup>1</sup> is more advanced than the one portrayed here. The CMS study included a full jet-reconstruction of each event, for both the leading and sub-leading jets. Therefore every event will have a unique frame. Additionally, as both di-jets are reconstructed for each event, cones can be created around the main and sub-leading jets, instead of just arcs. This gives additional precision to just where the quenching is located.

The full jet-reconstruction is an arduous task, as it is difficult to locate the sub-leading jet. The study concluded that jet quenching could be observed by creating projections from every track unto both di-jets, and measuring the jet. The sub-leading jet is not necessarily back-to-back to the leading jet, and its momentum can vary.

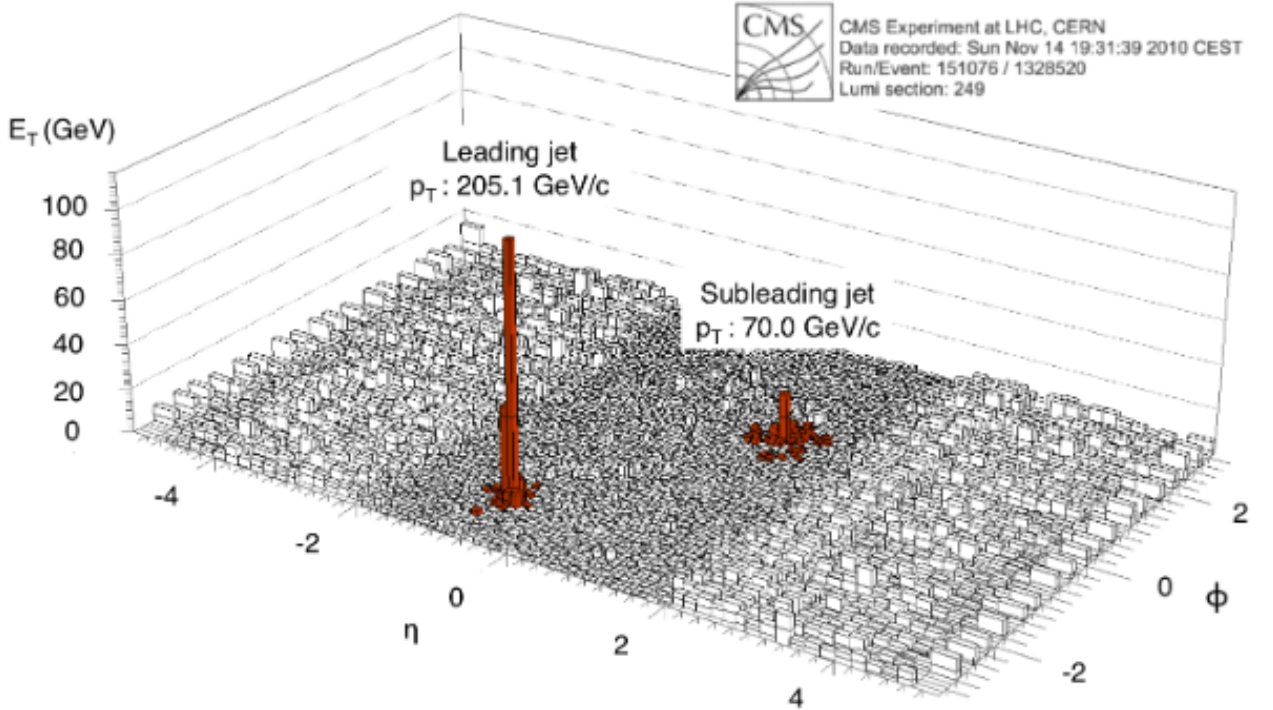


FIG. 18. Fully reconstructed di-jet event in CMS performed regarding jet quenching in Pb-Pb collisions<sup>1</sup>

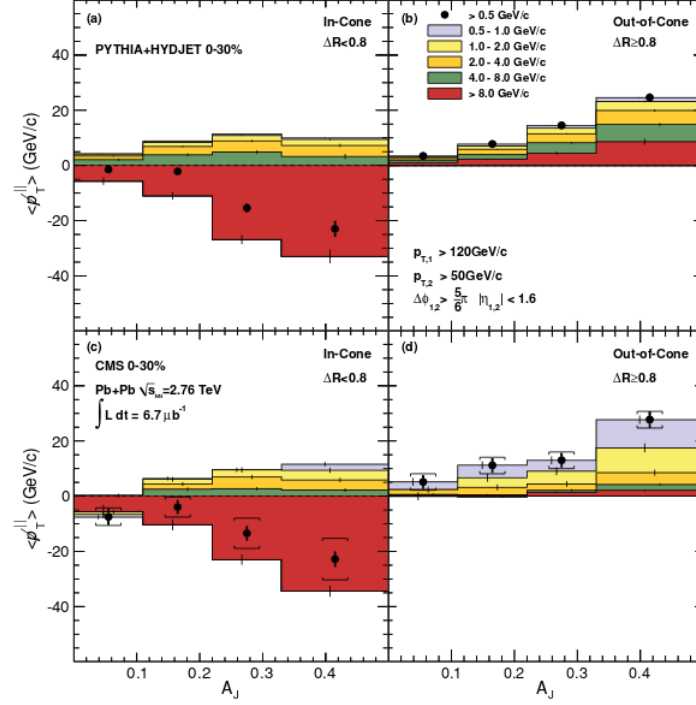


FIG. 19. Missing  $p_T$  projections from each area of Fig. 18 when taking the difference. Figures a) and b) represent simulated data in PYTHIA, where a) are the missing projections from the cone, and b) the missing projections from the bulk. Figures c) and d) represents the same kind of zones as a) and b), but are taken data.<sup>1</sup>

The results from the CMS portrayed the "missing"  $p_T$  projections in each each of the 4 zones in Fig. 16. this is done by graphing the average of  $p_{T\text{-proj}}$  against the value of  $A_j$ .  $A_j$  is defined as:

$$A_j = \frac{E_{j,1} - E_{j,2}}{E_{j,1} + E_{j,2}} \quad (12)$$

Where  $E_{j,1}$  and  $E_{j,2}$  are defined by the energy of the main

jet and secondary jet respectively. Hence, in the case of Fig. 18,  $E_{j,1} = 205.1$  GeV/c and  $E_{j,2} = 70.0$  GeV/c.

## V. RESULTS

The error analysis performed for the results in Fig. 22 through Fig 33 is the weighted sum of squares. With a weight of 1, the error in each bin is correlated to the square root of amount of entries in each bin.

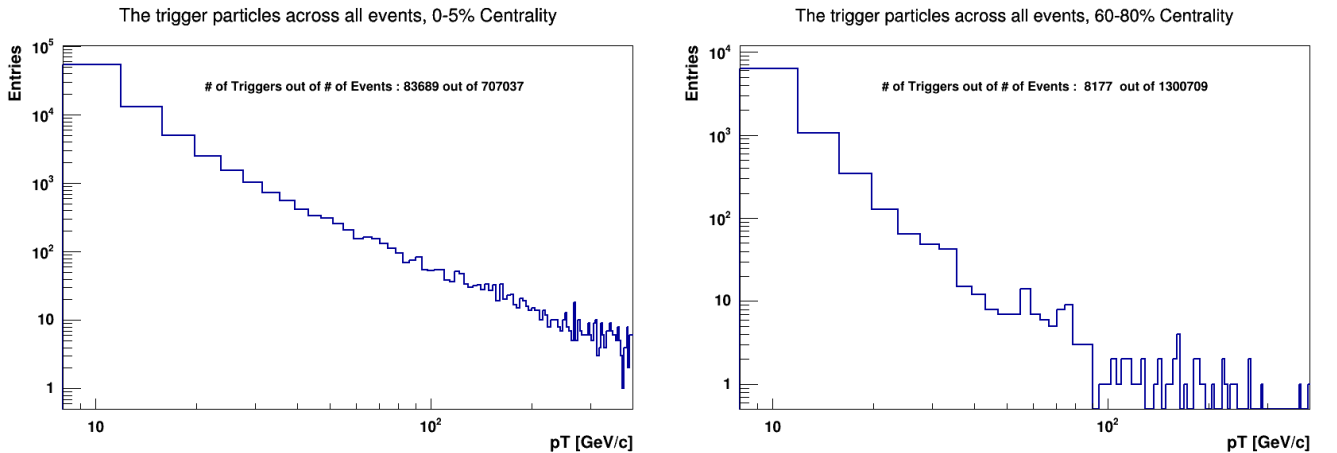


FIG. 20. The total amount of triggers from each respective centrality over 100 bins. The left figure represents the amount of trigger particles from Pb-Pb collisions at 0-5% centrality, whereas the right figure represents the amount of trigger particles from Pb-Pb collisions at 60-80% centrality

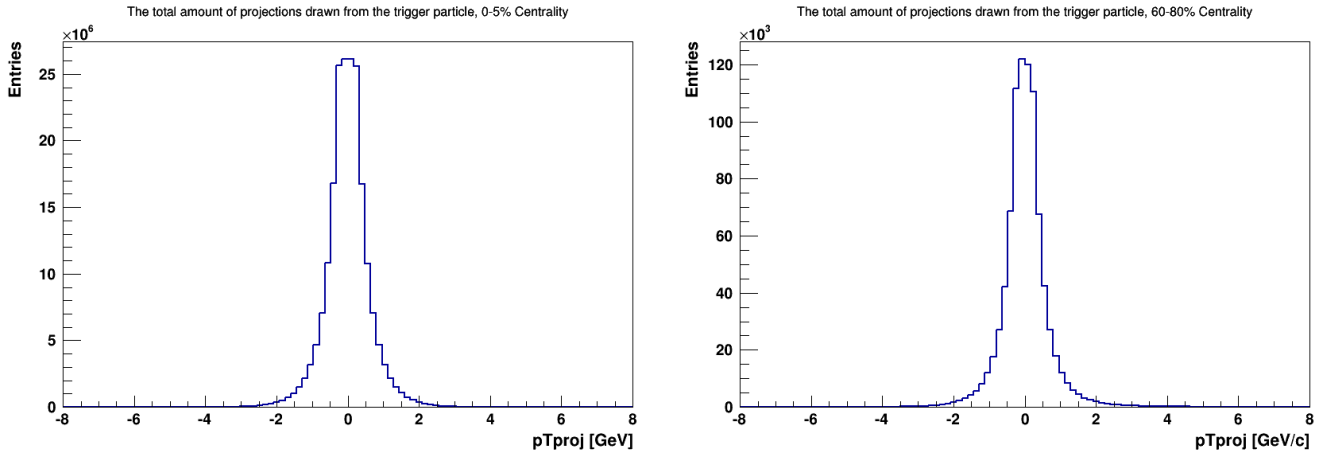


FIG. 21. The total amount of projections drawn, summed from all the trigger particles seen in Fig. 20 over 100 bins. The left figure represents the total amount of projections drawn from tracks from Pb-Pb collisions at 0-5% centrality, whereas the right figure represents the total amount of projections drawn from tracks from Pb-Pb collisions at 60-80% centrality

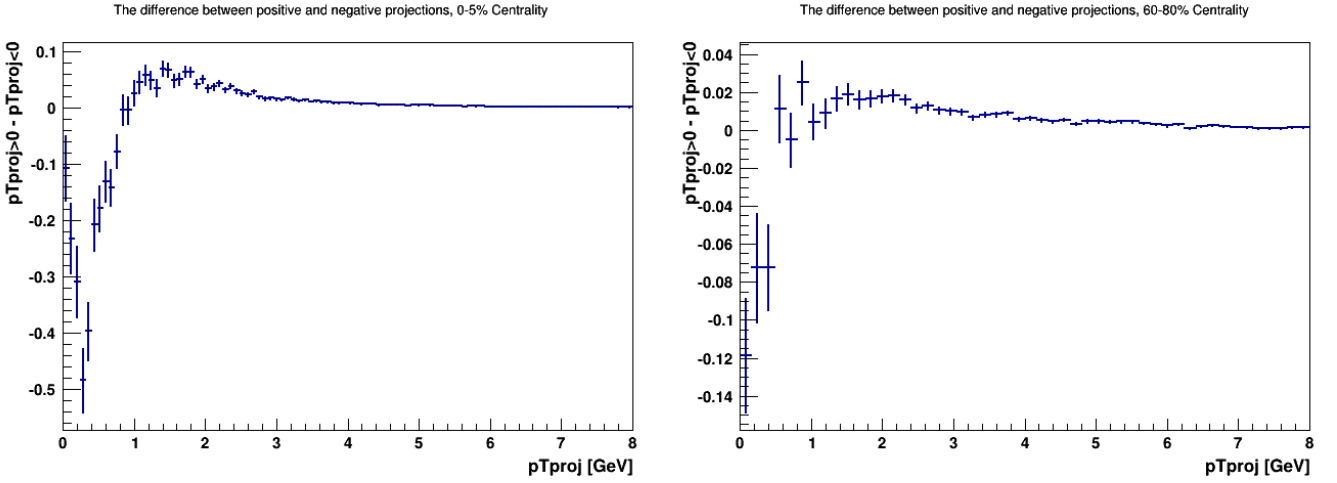


FIG. 22. The difference of the positive projections versus the negative ones. These histograms represent the difference between the projections of the tracks from zones 1+3 and 2+4. The left figure represents the difference between projections (100 bins) drawn from tracks from Pb-Pb collisions at 0-5% centrality, whereas the right figure represents the difference between projections (50 bins) drawn from tracks from Pb-Pb collisions at 60-80% centrality

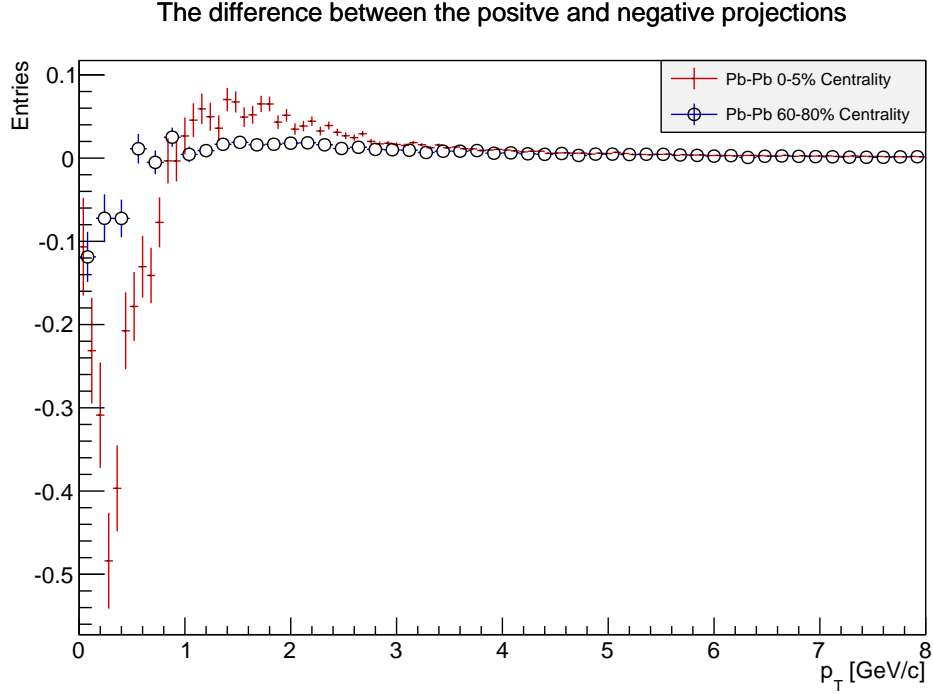


FIG. 23. The two figures from Fig. 22 on top of each other, in order to easier distinguish them. The red data points represent the left figure of fig. 21, whereas the blue data points represent the right figure of fig. 21

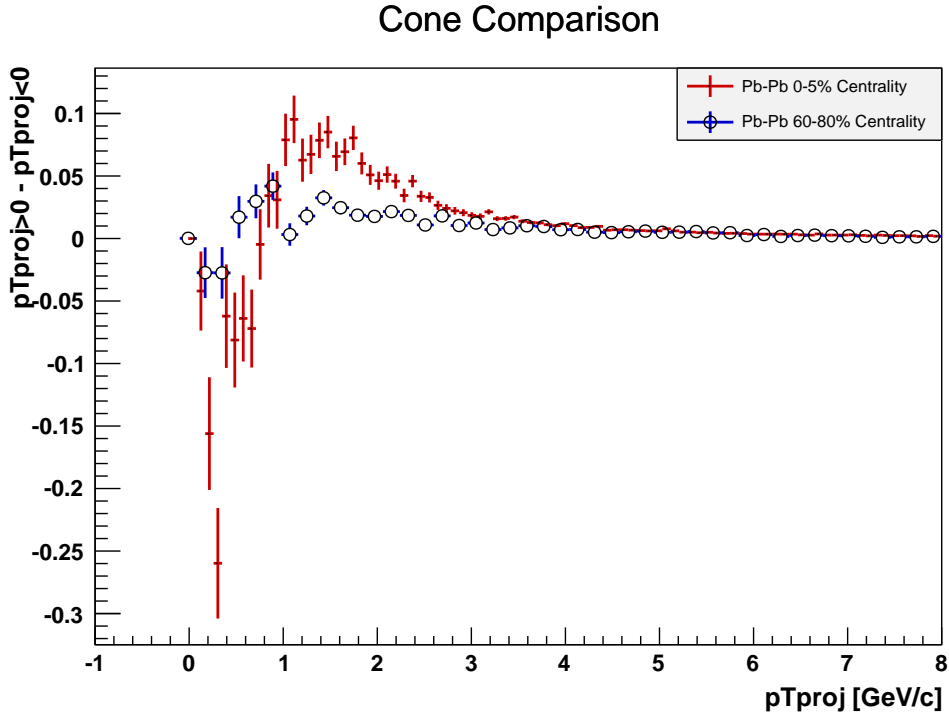


FIG. 24. Comparing the difference between positive and negative projections from tracks that are enclosed in the two cones (regions 1 and 2, Fig. 16). The red data (100 bins) represents the difference of projections for the Pb-Pb collisions with 0-5% centrality, whereas the blue data (50 bins) represents the difference of projections for the Pb-Pb collisions with 60-80% centrality.

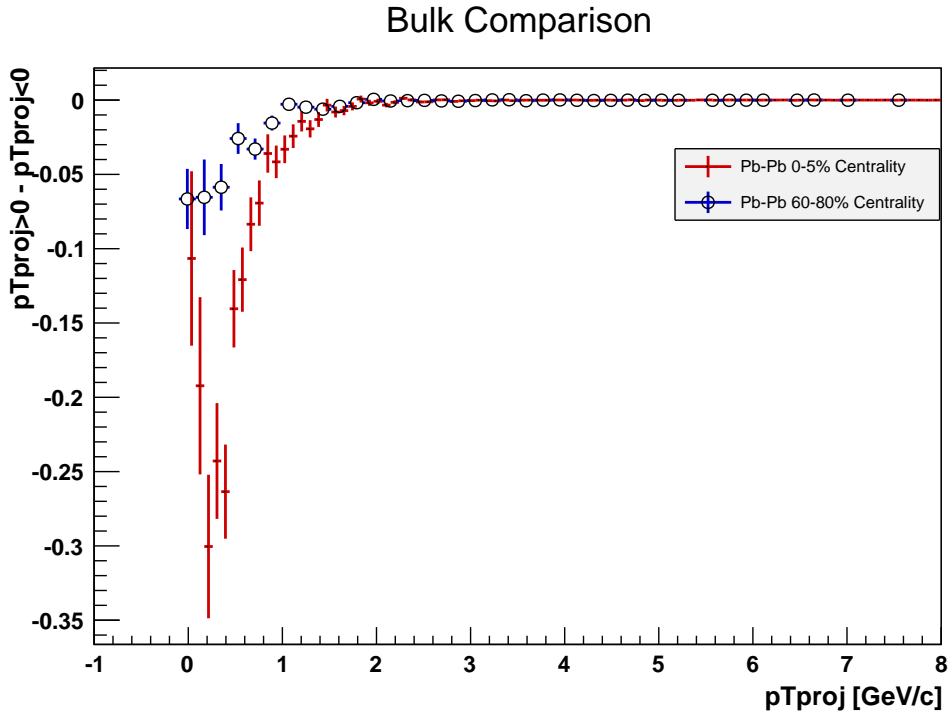


FIG. 25. Comparing the difference between positive and negative projections from tracks that are enclosed in the bulk (regions 3 and 4, Fig. 16). The red data (100 bins) represents the difference of projections for the Pb-Pb collisions with 0-5% centrality, whereas the blue data (50 bins) represents the difference of projections for the Pb-Pb collisions with 60-80% centrality.

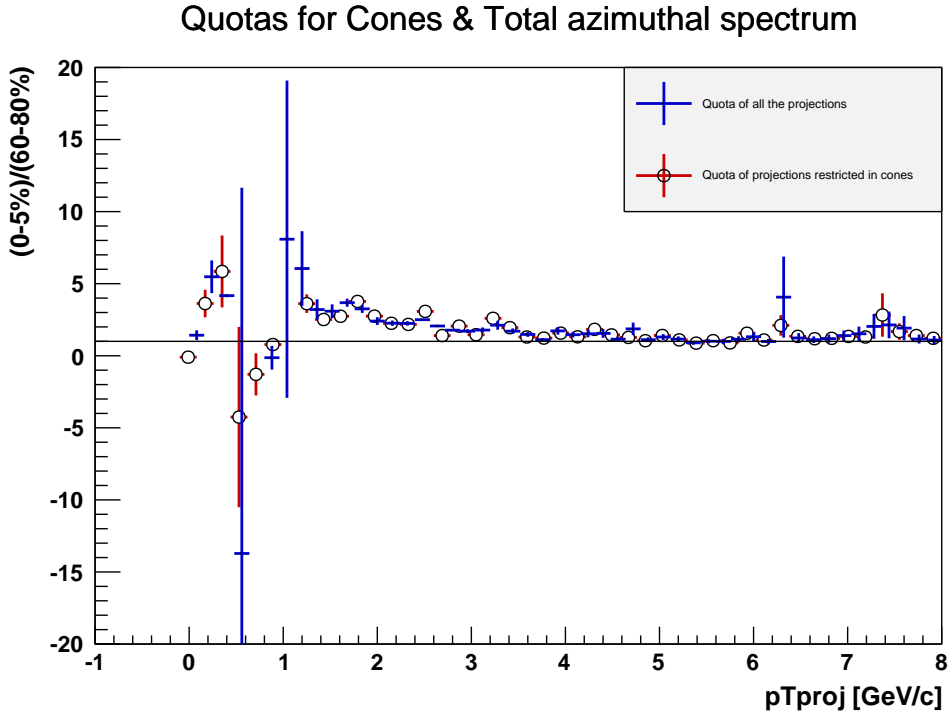


FIG. 26. Quota taken from the two different sets of data in Fig. 23 (Blue), together with the quota taken from the two different sets of data in Fig. 24 (Red).

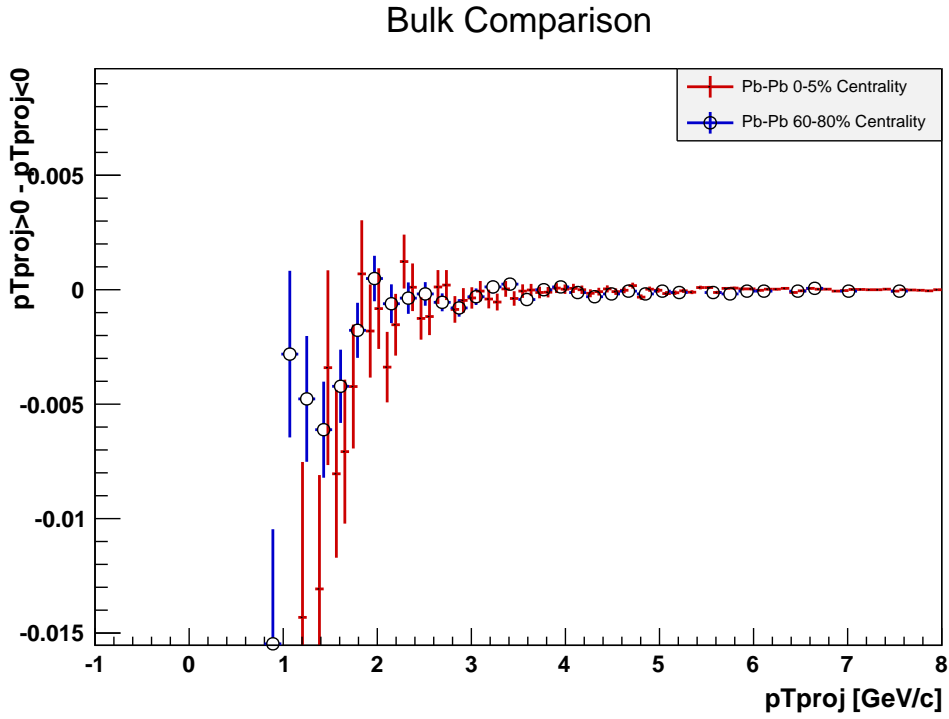


FIG. 27. Illustration displaying why the bulk quota is not included in Fig. 26; except for a minor amount of small projections, the data very tightly swings around 0. Taking the quote of two zero-like data lines would thus provide sporadic results.

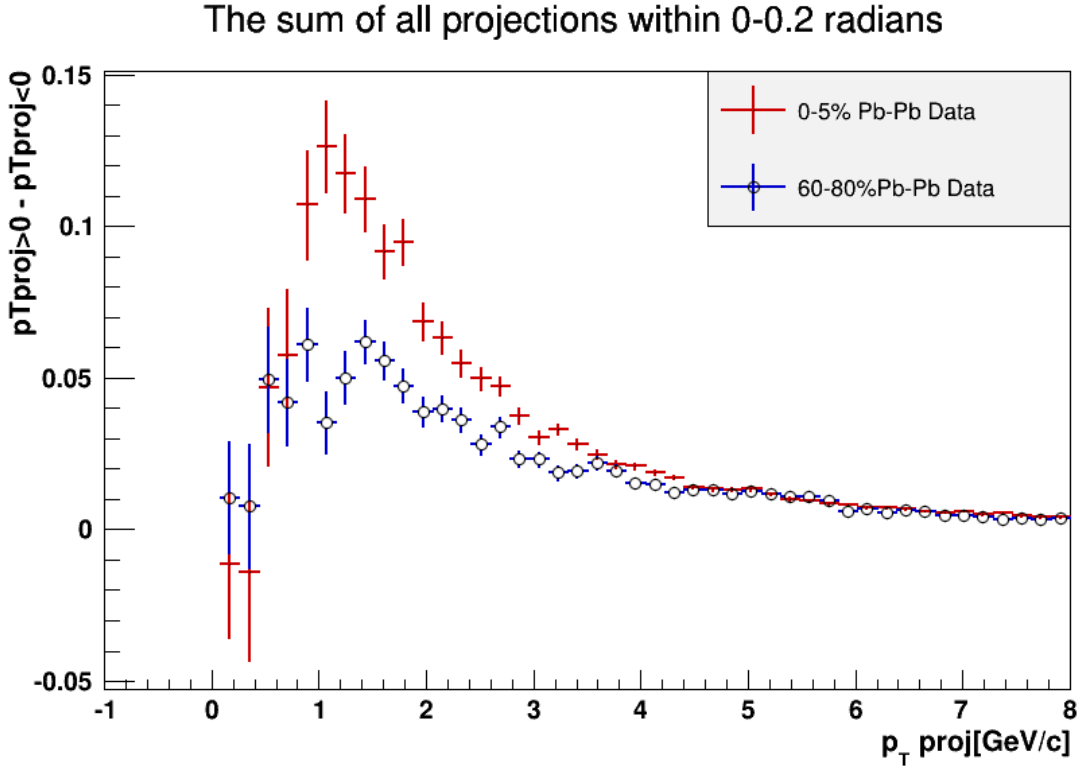


FIG. 28. The projections within the 0-0.2 radians away from the leading jet.

### The sum of all projections within 0.2-0.4 radians

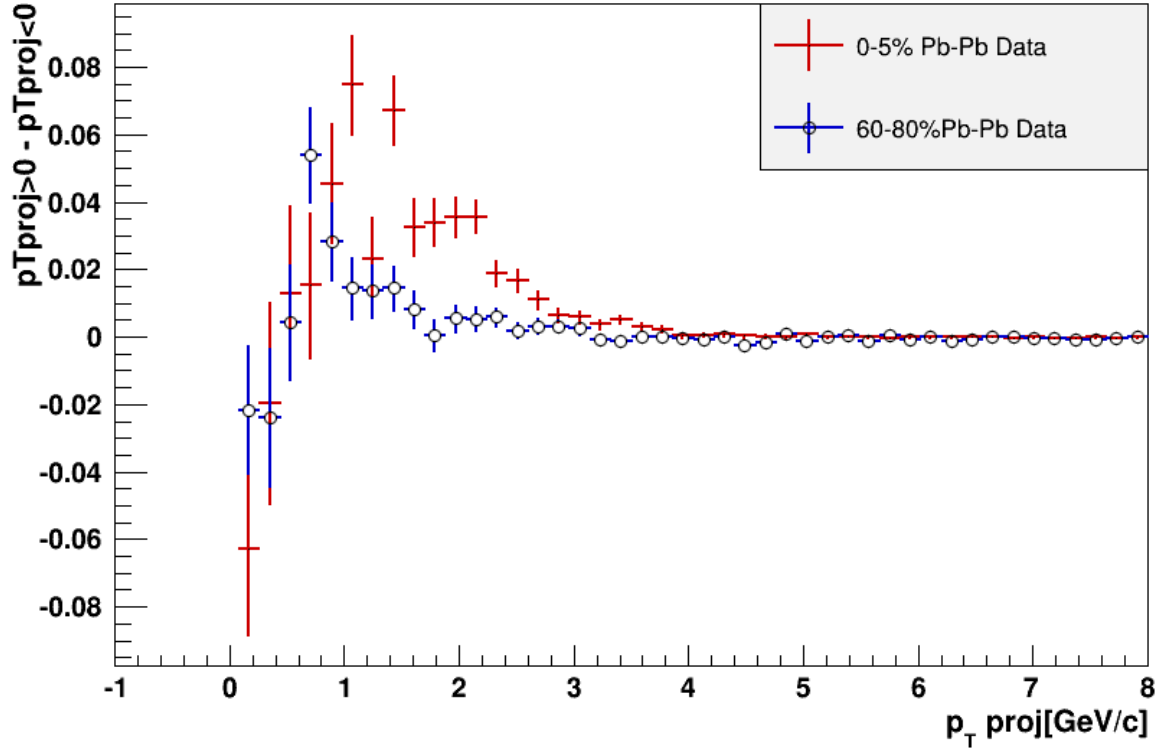


FIG. 29. The projections within the 0.2-0.4 radians away from the leading jet.

### The sum of all projections within 0.4-0.6 radians

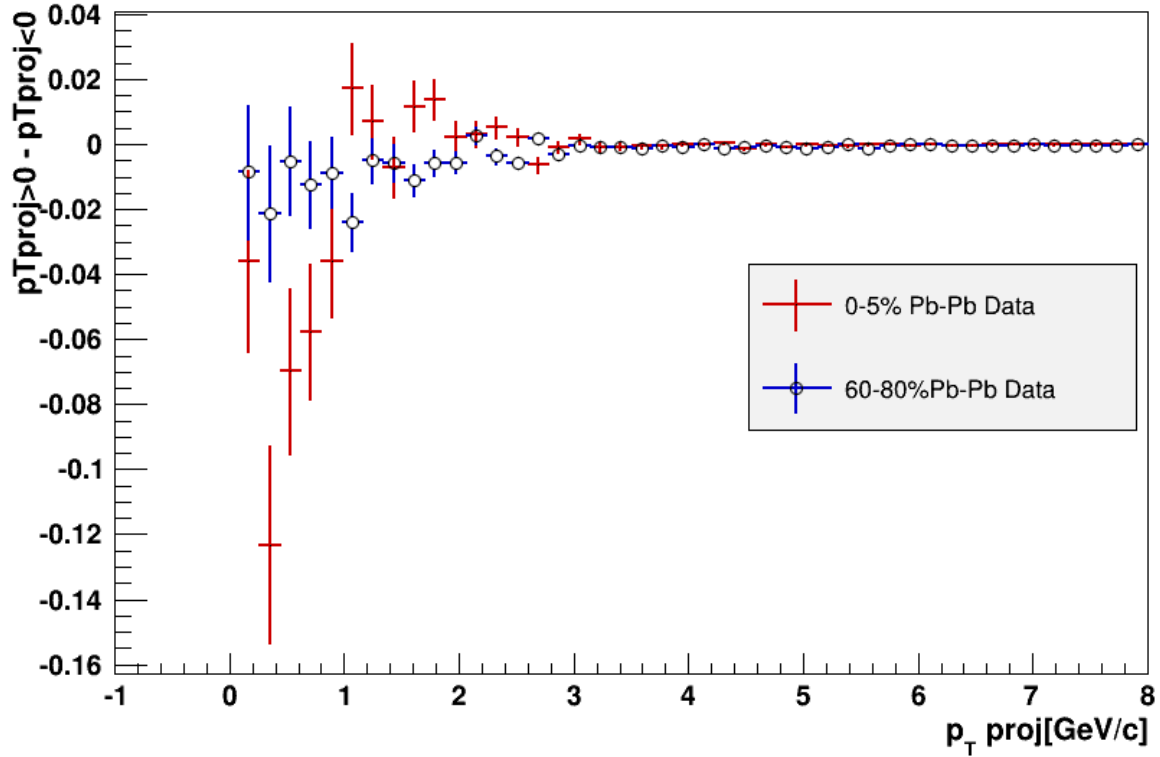


FIG. 30. The projections within the 0.4-0.6 radians away from the leading jet.

### The sum of all projections within 0.6-0.8 radians

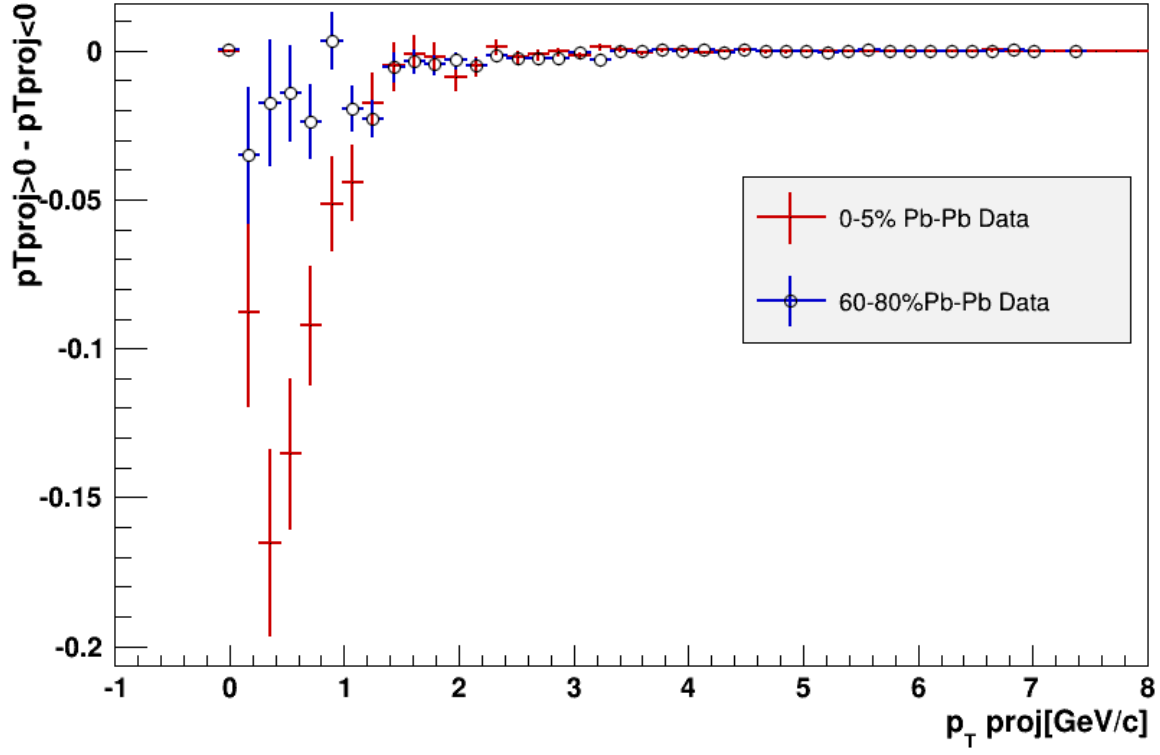


FIG. 31. The projections within the 0.4-0.6 radians away from the leading jet.

### The sum of all projections within 0.8-1 radians

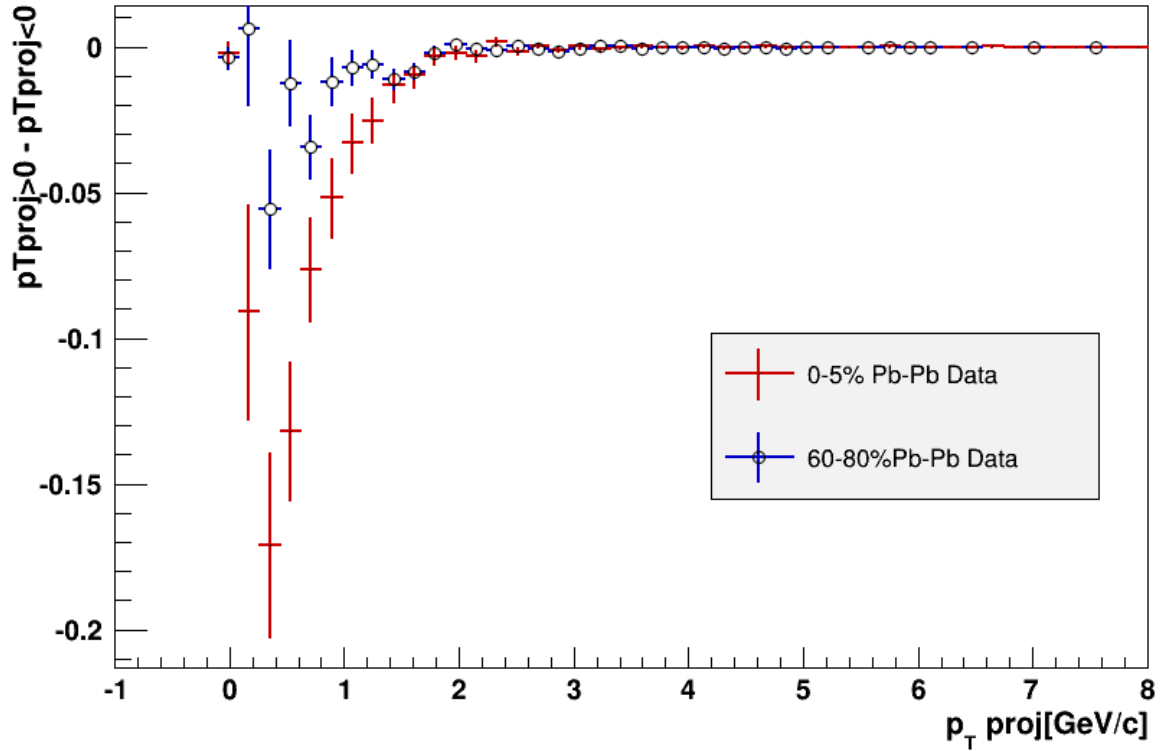


FIG. 32. The projections within the 0.6-0.8 radians away from the leading jet.

## VI. DISCUSSION

The number of trigger particles discriminated out of the total number of events are shown in Fig. 20. As can be expected, the ratio between the amount of trigger particles and events is much larger for the low centrality case. This is due to the fact that few 60-80% centrality collisions are energetic enough to pass the 8 GeV/ $c$  threshold. Other than difference of scale, the behavior of the two centralities are similar; the majority of the trigger particles lie around 8-15 GeV. Furthermore, the projections are drawn from every track unto the main trigger particle in Fig. 21. Again, the outcome is what is expected; combined with having a larger amount of trigger particles, the collisions at lower centrality contain more tracks, thus more projections are created.

While Fig. 21 displays that the characteristics of the data is fairly similar for the two centrality intervals, Fig. 22 distinguishes that there is a large density of negative, small  $p_T$  projections ( $< 1$  GeV/ $c$ ), as well as a small density of positive projections (ranges 1-3 GeV) for the 0-5% centrality case. Projections larger than 3 GeV/ $c$ , for both cases, either completely cancel out, or by observing Fig. 20 are small enough in number compared to the normalization factor (number of trigger particles). This can be seen even more clear when overlaying the two centralities in Fig. 23. The fact that there are significant regions of low  $p_T$  projections compared to the 60-80% baseline could indicate that the jets are quenched whilst traveling through the QGP.

Observing Fig. 24 and Fig. 25, it is possible to note more precisely where the unbalanced  $p_T < 1$  GeV/ $c$  and 1-3 GeV/ $c$   $p_T$  projections are located. The overshoot of small positive projections in Fig. 23 only correlates to the projections found in the leading cone in Fig. 24 (zone 1 in Fig. 16). The fact that the unbalanced, positive 1-3 GeV/ $c$  projections only lie in the cone for 0-5%, compared with that the projections are more balanced in the same region for 60-80%, heavily suggests that the aforementioned projections are due from jet quenching from the main jet. On the other hand, even though there are some negative  $p_T < 1$  GeV/ $c$  in the away-facing cone (negative values of Fig. 24), the majority of the small negative projections are associated to the away-facing bulk in Fig. 25 (zone 4 in Fig. 16). The huge disparity of negative  $p_T < 1$  GeV/ $c$  between the 0-5% and 60-80% in Fig. 25 indicates that they are due to jet quenching of the sub-leading jet.

This behavior is consistent with the results from Fig. 19. Since the two phenomena contrasts heavily between the two different centralities, this indicates the possibility of jet quenching. While the quenching alongside the main jet is located in the cones, the quenching alongside the sub-leading jet is spread out to the cones. This is due to the fact that the sub-leading jet has to traverse a larger swath of the QGP medium, and will thus have a larger angular distribution. This occurs as the the statistical likelihood of the gluon bremsstrahlung interacting with the medium is increased the longer it has to travel. This is further indicated by the angle between the 0-5% data and the 60-80% data in Fig. 25, revealing that the "tail"

of the sub-leading jet for 0-5%, as the two jets are not back-to-back, is wider than that of the 60-80% data.

In Fig. 26, the ratio between the projections inside the cone is compared to the ratio between all projections, for the two different centralities. Values larger than one would indicate an abundance in 0-5% projections, whereas values lower than one would indicate an abundance for 60-80% projections. Fig. 26 presents that there are a few  $< 1$  GeV/ $c$   $p_T$  projections that are more common in the baseline. On the other hand, one can note that large amounts of 1-3 GeV/ $c$   $p_T$  projections are more common in the 0-5% centrality data in contrast to the 60-80% data.

This ratio is rather needless to take for the bulk. By simply zooming in on the projections in the bulk (Fig. 27), it is made clear that there is almost no radiation emitted above 1 GeV/ $c$  in the bulk. So the quota would consist of mostly 0-like values, and have a chaotic distribution.

Lastly, Fig. 28 through Fig. 32 give a more detailed view of what happens inside the cones during the collisions. While the 60-80% data is more balanced, the 0-5% goes from having large quantities of positive 1-3 GeV/ $c$   $p_T$  projections close to the jet, and tapers off to having large quantities of negative  $< 1$  GeV/ $c$   $p_T$  projections further away from the jet. This further illustrates the "tail" that is created for the sub-leading jet during the central collisions.

## VII. CONCLUSION

While drawing projections from every particle track to the main jet, there is a large disparity between the results at 0-5% centrality compared to the 60-80% baseline for Pb-Pb collisions at  $\sqrt{s_{NN}} = 2.76$  TeV, detected in ALICE. The characteristics of the results from Fig. 24 and Fig. 25, especially when comparing the two different centralities, resembles the data from the measurements found in Fig. 19. Hence, the hypothesized method is viable; to be able to find signatures of jet quenching by only studying  $p_T$  of the jets and each particle track.

However, it is important to note that, even though there is a large disparity between the behavior of the central and peripheral collisions, the observed behavior does not necessarily correlate to jet quenching. Other factors, such as hydrodynamic flow (which is a soft scattering process), could be responsible for the low-momentum  $p_T$  projections. The 8 GeV/ $c$  trigger threshold is specifically set to ensure that the hard scattering process (defined by jets) dominates the soft scattering process, but one can not be entirely certain. In order for that, a more thorough analysis would have to be done that adjusts for flow. As mentioned in section (II-D), the scope of this thesis is too limited to account for flow.

Additionally, the study could be expanded in order to further observe the behavior of the projections inside the cones and bulks. One way of doing so would be to, for every point that there is a disparity between the data of the two centralities, identify if the disparity is a net result of either positive or negative projections.

## VIII. BIBLIOGRAPHY

- <sup>1</sup>S. Chatrchyan *et al.*, “observation and studies of jet quenching in pbb collisions at  $\sqrt{s_{NN}} = 2.76$  tev”, *Physical Review C*, vol. Volume 84, Issue 2, 2011.
- <sup>2</sup><http://www.physik.uzh.ch/groups/serra/images/SM1.png>. Last visited 10/12/2015.
- <sup>3</sup>G. Kane, “*Modern Elementary Particle Physics: The Fundamental Particles and Forces?*”. Perseus Publishing, 1993. Page 9.
- <sup>4</sup>G. Kane, “*Modern Elementary Particle Physics: The Fundamental Particles and Forces?*”. Perseus Publishing, 1993. Pages 105-112.
- <sup>5</sup>NIST. <http://physics.nist.gov/cgi-bin/cuu/Value?e>. Last visited 10/12/2015.
- <sup>6</sup>W. Florkowski, *Phenomenology of Ultra-Relativistic Heavy-Ion Collisions*. World Scientific Publishing Co. Pte. Ltd., 2010. Pages 6-7.
- <sup>7</sup>K. S. Krane, “*Introductory Nuclear Physics*”. John Wiley & Sons, Inc., 1988. Pages 721-724.
- <sup>8</sup>G. Shaw and B.R.Martin, *Particle Physics*. John Wiley & Sons, Inc., 1995. Page 158.
- <sup>9</sup>G. Kane, “*Modern Elementary Particle Physics: The Fundamental Particles and Forces?*”. Perseus Publishing, 1993. Pages 236-240.
- <sup>10</sup>G. Shaw and B.R.Martin, *Particle Physics*. John Wiley & Sons, Inc., 1995. Pages 164-165.
- <sup>11</sup>G. Shaw and B.R.Martin, *Particle Physics*. John Wiley & Sons, Inc., 1995. Page 160.
- <sup>12</sup>W. Florkowski, *Phenomenology of Ultra-Relativistic Heavy-Ion Collisions*. World Scientific Publishing Co. Pte. Ltd., 2010. Page 98.
- <sup>13</sup><http://www.pnas.org/content/102/24/8403.figures-only>. Fig 3. Last visited 10/12/2015.
- <sup>14</sup>E. M. Riordan, “The Discovery of quarks”, *Science*, vol. 256, 1992. Pages 1287-1293.
- <sup>15</sup><http://pdg.web.cern.ch/pdg/cpep/color.html>. Fig 3. Last visited 10/12/2015.
- <sup>16</sup>G. Kane, “*Modern Elementary Particle Physics: The Fundamental Particles and Forces?*”. Perseus Publishing, 1993. Page 169.
- <sup>17</sup>A. K. Chaudhuri, “*A Short Course on Relativistic Heavy-Ion Collisions*”. Institute of Physics Publishing, 2014.
- <sup>18</sup>M. L. Miller *et al.*, “Glauber modeling in high energy nuclear collisions.” <http://arxiv.org/pdf/nuc1-ex/0701025v1.pdf>, 2007. Last visited (10/12/2015).
- <sup>19</sup>K. Reygers, “Glauber monte-carlo calculations for au+au collisions at  $\sqrt{s_{NN}} = 200$  gev.” [http://www.phenix.bnl.gov/~\\$enterrria/tmp/glauber/glauber\\$\\_\\$auau\\$\\_\\$200gev.pdf](http://www.phenix.bnl.gov/~$enterrria/tmp/glauber/glauber$_$auau$_$200gev.pdf), 2003. Last visited (10/12/2015).
- <sup>20</sup>G. Kane, “*Modern Elementary Particle Physics: The Fundamental Particles and Forces?*”. Perseus Publishing, 1993. Page 180-181.
- <sup>21</sup>W. Florkowski, *Phenomenology of Ultra-Relativistic Heavy-Ion Collisions*. World Scientific Publishing Co. Pte. Ltd., 2010. Pages 8-11.
- <sup>22</sup>E. Stenlund. Personal Correspondance.
- <sup>23</sup>STAR-Collaboration. Personal Correspondance. Data from the STAR Collaboration, modified by E. Stenlund.
- <sup>24</sup>B. Abelev *et al.*, “transverse momentum distribution and nuclear modification factor of charged particles in p+pb collisions at  $\sqrt{s_{NN}} = 5.02$  tev”, *Physical Review Letters*, vol. 110, Iss 8, 2013.
- <sup>25</sup>V. Visclavičius, “Azimuthal angular description of jet quenching at high  $p_T$ ,” Master’s thesis, Lund University, 2013.
- <sup>26</sup>W. Florkowski, *Phenomenology of Ultra-Relativistic Heavy-Ion Collisions*. World Scientific Publishing Co. Pte. Ltd., 2010. Page 33-35.
- <sup>27</sup>W. Florkowski, *Phenomenology of Ultra-Relativistic Heavy-Ion Collisions*. World Scientific Publishing Co. Pte. Ltd., 2010. Pages 27-28.
- <sup>28</sup><http://home.cern/about>. Last visited 10/12/2015.
- <sup>29</sup><http://cds.cern.ch/record/1092437/files/CERN-Brochure-2008-001-Eng.pdf>. Last visited 10/12/2015.
- <sup>30</sup>R. Schicker in “*4th Workshop on Elastic and Diffractive Scattering (EDS Blois Workshop)*” *Frontiers of QCD: From Puzzles to Discoveries*, (Quy Nhon, Vietnam), Dec. 15-21.
- <sup>31</sup><http://aliceinfo.cern.ch/Public/en/Chapter2/Chap2Experiment-en.html>. Last visited 10/12/2015.
- <sup>32</sup>J. Baechler, “The alice tpc.” <http://www.physi.uni-heidelberg.de/~dwiedner/DetektorenBeschleunigerWS1112/ALICE%20TPC.pdf>. Last visited 14/12/15.
- <sup>33</sup>J. Alme *et al.*, “The alice tpc, a large 3-dimensional tracking device with fast readout for ultra-high multiplicity events,” *Nuclear Instruments and Methods in Physics Research Section A*, vol. Volume 622, Iss 1, 2010.